The Star-Formation Properties of Nearby AGN in the Observed and Simulated Universe: BAT vs EAGLE

THOMAS MATTHEW JACKSON

How to cite:

JACKSON, THOMAS MATTHEW (2018) The Star-Formation Properties of Nearby AGN in the Observed and Simulated Universe: BAT vs EAGLE. Masters thesis, Durham University.

The Star-Formation Properties of Nearby AGN in the Observed and Simulated Universe: BAT vs EAGLE

Thomas M. Jackson

A Thesis presented for the degree of
Master of Science by Research

Centre for Extragalactic Astronomy
Department of Physics
Durham University
United Kingdom

September 2018

Declaration

The work in this thesis is based on research carried out in the Centre for Extragalactic Astronomy, Department of Physics, Durham University, United Kingdom. No part of this thesis has been submitted elsewhere for any other degree or qualification and it is all my own work unless referenced to the contrary in the text.

Contents

Abstract **5**

1 Introduction **6**

1.1 Active Galactic Nuclei 6

1.2 AGN and Star Formation 8

1.3 AGN and Simulations 9

1.4 This Thesis 10

2 Observational Sample **11**

2.1 X-ray selection 11

2.2 IR and Optical Counterpart Data 13

3 Simulations **15**

3.1 EAGLE 15

3.2 Simulated Comparison Sample 17

4 Methods **19**

4.1 SED Fitting of the BAT AGN using Fortes Fit 19

4.2 Flux and Volume Matching the Samples 21

4.3 Use of the Merger Trees within EAGLE 23

4.4 High Time Resolution Data in EAGLE 25

4.5 Linmix Bayesian Fitting Routine 26

5 Results **28**

5.1 Trends in the Full Swift-BAT AGN Sample 28

5.2 Comparison of BAT AGN and EAGLE AGN 30

5.3 SFR Distributions from Monte-Carlo Methods 32

5.4 Comparison of sSFR distributions 33

5.5 The Evolution of AGN Host Galaxy Properties in EAGLE 36

5.6 Quasar-like episodes in EAGLE 38

6 Discussion **42**

6.1 Comparison of BAT and EAGLE AGN host galaxy properties 42

6.2 How the host galaxies of AGN selected at different epochs differ 44

6.3 How quasar-like episodes affect Star Formation in EAGLE 45

7 Conclusion **46**

APPENDICES **50**

A SED fits **50**

B Initial Comparison Graphs **52**

C Colour-Magnitude diagram **53**

The Star-Formation Properties of Nearby AGN in the Observed and Simulated Universe: BAT vs EAGLE

Thomas M. Jackson

Abstract: In this thesis we present data from 272 low redshift, hard X-ray (14 - 195 keV) selected Active Galactic Nuclei (AGN) taken from the Swift-BAT all sky survey. We calculated Star Formation Rates (SFRs) and Specific Star Formation Rates (sSFRs) via Spectral Energy Distribution fitting in the optical and infra red parts of the elctromagnetic spectrum. The host galaxy properties of a sub-sample (72 AGN) were compared to a flux and volume matched sample of AGN from the EAGLE hydrodynamical simulations in order to verify how accurately the simulations can reproduce the observational data, including some Monte-Carlo methods. We find Anderson-Darling test agreements in the SFR distributions of 20% (45% in the MC methods), however $< 1\%$ in the sSFR distributions. This difference is driven by an on average underprection of the sSFR per stellar mass bin in EAGLE. The X-ray luminosity distributions are also poorly reproduced (1.8% agreement). We postulate that the difference in X-ray luminosities is due to the short timescales on which AGN activity varies and that general differences may be accounted for due to the compton thick population. We find that the median of the sSFR distributions of both our observed and simulated AGN lie below the sSFR main sequence, in agreement with previous studies. We also explore the evolution of average AGN host galaxy properties within EAGLE in high time resolution data (1 Myr steps) over the last 700 Myr and throughout cosmic time up to $z = 5$ in low time resolution steps (21 snapshots). This firstly reveals factors in EAGLE such as critical masses ($M_* \sim 10^{10}$ $M_\odot$) at which AGN feedback starts to have a significant effect on the host galaxy, mainly via the quenching star formation. It secondly reveals the effect of quasar-like events ($L_{BOL} > 10^{45}$ erg s^{-1}) which can significantly quench star formation. We also investigate the cosmic evolution of average host galaxy properties of two differently selected populations of AGN in EAGLE. We find that galaxies selected on similar criteria from different epochs show similar behaviours but display different average host galaxy properties in the present day.

Chapter 1

Introduction

1.1 Active Galactic Nuclei

It is generally accepted that all massive galaxies contain a Supermassive Black Hole (SMBH) residing at their centre (Richstone et al., 1998). Active Galactic Nuclei (AGN) are different in comparison to the average galaxy population as they have increased nuclear activity in their central region around this SMBH (Alexander and Hickox, 2012). A diagram of the classical model used to explain this phenomena is shown in Figure 1.1 [1].

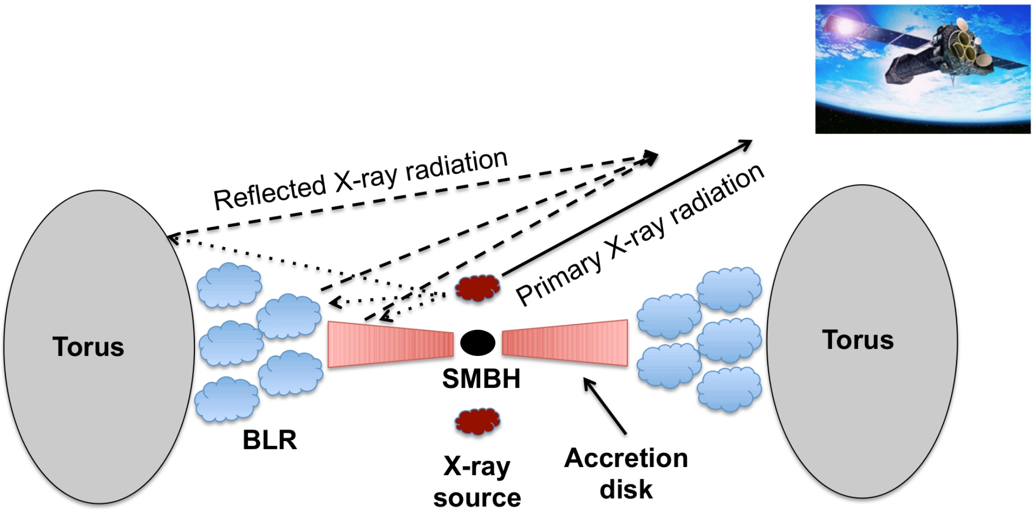

Figure 1.1: A classical model of an AGN. The SMBH with a surrounding accretion disk can be seen in the centre, surrounded by a dusty Torus farther out. These components of the AGN occupy the inner few pc of the host galaxy.

---

[1] `http://www.isdc.unige.ch/~ricci/Website/AGN_in_the_X-ray_band.html`

This increased nuclear emission is thought to be caused by the infall of gas towards the central SMBH, which can be delivered either internally from the inner parts of the host galaxy or externally from interacting galaxy neighbours, the dark matter halo or (intra) cluster gas. As the gas falls inwards towards the centre of the gravitational potential well, it loses gravitational potential energy, which is converted into kinetic energy. This material then forms an accretion disk around the SMBH where, due to internal frictional processes, the kinetic energy is converted into heat energy. The gas in the accretion disk therefore radiates like a series of black bodies, peaking in the Ultra-Violet (UV) part of the Electromagnetic (EM) spectrum. Other processes contribute to this increased nuclear activity as well. The surrounding dusty torus emits in the Infra-Red (IR) part of the EM spectrum and an additional X-ray component is also seen as power law continuum emission which arises from processes such as Thompson upscattering of photons off the accretion disk (See Alexander and Hickox (2012) for review).

These processes of converting gravitational potential energy into kinetic and then heat energy are many times more efficient than nuclear fusion. Therefore, even a SMBH accreting at a relatively low rate can produce a great amount of power. An accretion rate of 1 $M_\odot$ yr^{-1} may allow the AGN to attain a greater luminosity than its entire host galaxy, sometimes appearing as a point source in optical observations rather than the extended emission profile generally expected for a galaxy (Alexander and Hickox (2012)). Therefore, although these AGN components are physically many orders of magnitude smaller than the host galaxy itself (sub-parsec scales compared to the kpc scales of the host galaxy), the energetic scales are similar. If the AGN produces a similar or greater amount of power than the host galaxy around it, we may find that some areas of the galaxy may be dominated by the energy from the AGN. The AGN may then, have some sort of influence on their host galaxies, whereby energy radiated by the accreting SMBH is injected back into the host galaxy influencing various host galaxy properties. This is the theory of AGN feedback.

Indeed many studies have found evidence linking average galaxy population properties to their central SMBH. This includes the black hole mass - bulge mass relationship (Häring and Rix (2004)) and the $M_{\cdot}$ - σ relation (see Kormendy and Ho (2013) for review). In these studies black hole masses can be inferred from a number of different methods; reverberation mapping, water masers and gas or stellar dynamics (See van den Bosch (2016) and references herein). Similarly there are a number of methods for measuring the host galaxy properites, e.g bulge mass (via the virial theorem) or line of sight velocity dispersions. (See Courteau et al. (2014) for a review of scaling relations). Another connection is the similar behaviour of the evolution of the average cosmic Star Formation Rate (SFR) and Black Hole Accretion Rate (BHAR) (Aird et al. (2015)) which increase together, peaking at $z \sim 2$ before decreasing together again up to the present day. Although this indirect evidence seems to indicate a co-evolution between a galaxy and it's central SMBH, no direct evidence has yet been found.

Star formation shares the same raw fuel as an accreting SMBH, cold gas. It is also the primary process by which galaxies grow in stellar mass (discounting mergers or other similar processes), much like accretion is the primary process by which SMBHs grow. This has made star formation a prime candidate in the search for imprints of AGN feedback and is the primary focus of our research.

1.2 AGN and Star Formation

Many studies seem to agree on a flat trend between the average host galaxy Star Formation Rate (SFR) as a function of AGN luminosity for moderate luminosity AGN (10^{43} erg s^{-1} < L_{BOL} < 10^{45} erg s^{-1}) (Rosario et al. (2012), Stanley et al. (2015), Shimizu et al. (2017)). They also agree that the average SFR of AGN host galaxies evolves with redshift at all AGN luminosities (Harrison et al. (2012), Rosario et al. (2012), Stanley et al. (2015)), whereby the average SFR increases with redshift up to $z \sim 2$. This redshift evolution of the average SFR is expected as this behaviour is also observed in the average galaxy population (Schreiber et al., 2015).

Because AGN and star formation rely on cold gas as fuel, we may expect the two processes to show a positive correlation. The observed flat relation between SFR and AGN luminosity in moderate luminosity AGN therefore may be an unexpected result. An initial conclusion may be that AGN activity and Star formation are not connected. Hickox et al. (2014), however, argue that the reason we do not see any relation, even when we may expect one, is due to the different timescales upon which luminosity due to star formation and AGN luminosity vary. The AGN luminosity in the optical/UV/X-ray is expected to vary on the order of hours/days/years due to instabilities in the accretion disk. Significant differences in the luminosity, driven by changes in the average accretion rate, are expected of the order of a Myr (See Sartori et al. (2018)). The luminosity due to star formation varies on the order of 100 Myr. Due to the relatively short timescales on which AGN activity varies, any expected correlation over a general population of AGN galaxies is washed out.

As studies approach the high luminosity end of their respective AGN samples ($L_{BOL} > 10^{45}$ erg s^{-1}), however, inconsistent results emerge. Some studies argue for a positive trend in the average SFR as function of AGN luminosity (e.g Netzer (2009), Rosario et al. (2012)), some for a continuation of the flat trend seen in moderate luminosity AGN (e.g Shimizu et al. (2017)) and some for a negative trend (e.g Page et al. (2012)). These disparities arise for two reasons. Firstly AGN at such high luminosities are increasingly rare and hence introduce statistical biases. Secondly the estimations of SFRs can become increasingly contaminated by AGN emission at the high end of the luminosity function, causing the SFR to be over-estimated.

One recent study carried out by Stanley et al. (2017), using a large sample ($\sim$ 3000 AGN) with reliable photometry and SFR estimation techniques, showed that there is a slight positive trend in the SFR in high luminosity AGN ($L_{BOL} > 10^{45}$ erg s^{-1}). This trend, however, is shown to be driven by stellar mass effects. Higher luminosity AGN tend to reside in more massive galaxies, which have on average higher SFRs. In the local universe, however, there are very few high luminosity AGN and we can expect to recover the observed flat relationship.

1.3 AGN and Simulations

An alternative approach that some researchers employ is the use of cosmological simulations. Indeed, most successful simulations require AGN feedback in order to reproduce multiple properties of the observed universe, indicating that AGN feedback may play a significant role in our universe. Some of these properties include the colour bi-modality of galaxies in the colour magnitude plane, the black hole–spheroid relationship and the metallicity of the intergalactic medium (Alexander and Hickox (2012), Fabian (2012), Harrison (2017)). One such property is the present day stellar mass function (Bower et al. (2006), Croton et al. (2006)). In this specific case, when AGN feedback is not included, an overabundance of high mass galaxies ($M_* > 10^{12}$ $M_\odot$) are found in the simulations which are not observed in our local universe. Within the simulations AGN feedback is implimented in order to regulate how much mass galaxies can assemble. This works by slowly quenching star formation in galaxies above a mass $M_* \gtrsim 10^{10}$ $M_\odot$. This therefore reduces the number density of very high mass galaxies ($M_* > 10^{12}$ $M_\odot$). Depending on the simulation the feedback can be delivered thermally (Schaye et al., 2015), mechanically (Hardcastle, 2018) or using a mixture of both (Dubois et al., 2016). In order to find evidence for AGN feedback we need to find observable properties which are affected by AGN feedback. One of these properties, the width of the sSFR distributions, is outlined in the work of Scholtz et al. (2018), the basis of this research.

1.4 This Thesis

This research builds on the work carried out by Scholtz et al. (2018), who compared AGN at high redshift ($1.5 < z < 3.2$) to the EAGLE hydrodynamical simulations. In order to find the imprints of AGN feedback on star formation, Scholtz et al. (2018) initially compared EAGLE models with and without AGN feedback. They found that AGN feedback quenched star formation in higher mass galaxies ($M_* > 10^{10}$ $M_\odot$), thereby broadening the sSFR distributions of the entire galaxy population. Next they also found good agreement between the sSFR distributions of their observational sample and a matched comparison sample from the EAGLE models incorporating AGN feedback, indicative of AGN feedback in the observable universe. This project compares the star forming properties of a volume matched, flux matched sample of local AGN galaxies to the EAGLE hydrodynamical simulations in order to verify if these results are reproduced in the local universe. This has the advantage that observationally, SFRs are much easier to estimate for observed galaxies than those at high redshift. To investigate how much the selection of AGN affects the present day properties of AGN host galaxies, we also investigate the cosmic evolution within EAGLE of two AGN samples, one used in this work and the EAGLE comparison sample used in Scholtz et al. (2018). Finally to discover how EAGLE quenches star formation via AGN feedback, we explore the effect of quasar-like events ($L_{BOL} > 10^{45}$ erg s^{-1}) in high-time resolution data on the star forming properties of host galaxies.

This thesis will continue by outlining the observational sample in Chapter 2. In Chapter 3 we give an outline of the EAGLE hydrodynamical simulations and the comparison sample used in this research. Chapter 4 contains explanations of the methods used in this analysis. In Chapter 5 we present the results of the research. This is a followed by a discussion and interpretation of the results found in Chapter 6. Finally we give a conclusion in Chapter 7.

Chapter 2

Observational Sample

In this section we will describe the observational data sample used in this project. This will include the X-ray selection of AGN and the data collection of the counterpart photometry in the IR and optical.

2.1 X-ray selection

AGN can be identified in many different bands of the EM spectrum such as the IR or the optical. Selection of AGN in the hard X-ray band ($E \gtrsim 10$ keV), however, can be advantageous. Firstly, there are relatively few sources other than AGN which produce hard X-ray emission, reducing the chance of contamination in both sample selection and luminosity measurements. Secondly, absorption of radiation in the hard X-ray band only occurs in high hydrogen cloud column densities along the line of sight ($\mathrm{n}_{H_2} \gtrsim 10^{24}$ cm^{-2}). Other parts of the EM spectrum such as the UV or optical are blocked at much lower column densities. X-ray selection, especially in the hard regime ($E \gtrsim 10$ keV) can therefore lead to the discovery of new, highly obscured AGN (Koss et al. (2010)). For these reasons, we use the NASA Swift satellite's Burst Alert Telescope (hereafter Swift-BAT)[1], which operates in the hard X-ray band (14 - 195 keV), to select our AGN.

Although not as sensitive as other X-ray surveys such as Chandra (Alexander et al. (2001)), which observes in the soft X-ray band (0.2 - 10 keV), the advantage of Swift-BAT is its all sky coverage and hard X-ray band energy (14 - 195 keV). This firstly provides a relatively unbiased, large sample of AGN compared to IR or radio selection. This allows for an easy

---

[1] `https://swift.gsfc.nasa.gov/`

comparison to EAGLE as heavily obscured AGN remaining undetected do not need to be as heavily accounted for as with lower X-ray energies. Secondly, because we constrain this research to the local universe, objects with the same X-ray luminosity have higher fluxes than those at higher redshifts, and hence can still be observed with the lower sensitivities of BAT compared to other surveys.

Biases can be caused by the redshift evolutionary effects observed in the BHARs and SFRs (e.g Aird et al. (2015), Schreiber et al. (2015)). In order to minimise these effects (which may affect results) but still contain a statistically significant number of AGN in our sample, a redshift cut-off of 0.05 was applied to all sources in the Swift-BAT 58 month catalogue[2]. 313 AGN fulfil this criterion, providing our parent BAT sample. The completeness of this sample is not stated in the literature and beyond the scope of this project for calculating, we assume however that this is relatively low (less than a few %) and should not majorly impact our results.

In order to reduce the contamination that galactic sources may have on any measurements in both the hard X-ray and the optical and IR photometry described in Section 2.2, AGN within ± 10° of the Galactic plane were then removed from the parent AGN sample. To attain more accurate measurements of the X-ray luminosities and redshifts than those given in the catalogues, the data were matched to the BASS survey[3]. The BASS survey is follow up optical and IR spectroscopic survey of Swift-BAT sources, calculating the redshift from the shift in the [OIII] emission line and collecting the X-ray luminosities from archival data from multiple sources such as Chandra. The distribution of our this sample (hereafter full BAT AGN sample) in right ascension (RA) and declination (DEC) can be seen in the left panel of Figure 2.1.

As seen, once accounting for the Milky Way the spatial distribution is fairly, but not completely, uniform. The redshift and X-ray luminosity ($L_{14-195KeV}$) distribution of the full BAT AGN sample can be seen in the right panel of Figure 2.1. This displays the flux sensitivity of the instrument clearly and the biases towards higher luminosities that it introduces as we observe sources farther away. This is something that needs to be accounted for when making comparisons to the simulations.

---

[2] `https://swift.gsfc.nasa.gov/results/bs58mon/`

[3] `https://www.bass-survey.com/`

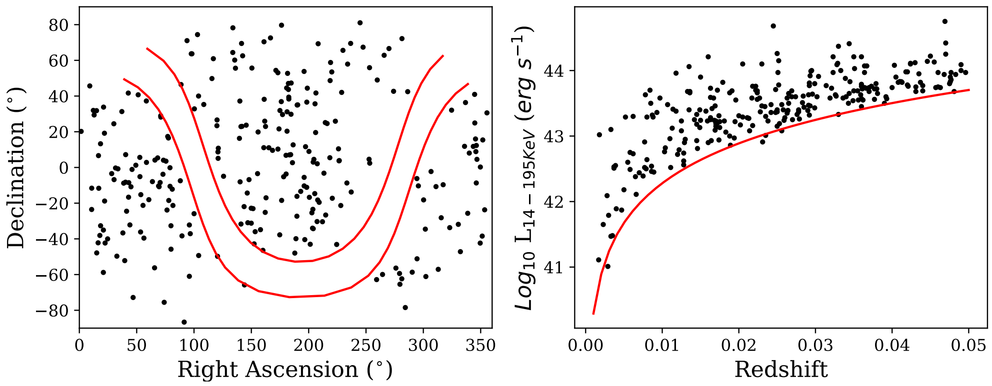

Figure 2.1: The left panel shows the distributions of the full BAT AGN sample (black points) used in this project in RA and DEC and the 10° limits from the central Milky way plane as red lines. The right panel shows the distribution in redshift and X-ray Luminosity ($L_{14-195KeV}$) with the flux limit represented by a red line.

2.2 IR and Optical Counterpart Data

Host galaxy properties such as masses and SFRs can be estimated from Spectral Energy Distribution (SED) fitting. This process as well as the associated physical phenomena are described further in Section 4.1. In order to fit an SED to an AGN to estimate these properties, multiple photometric data points spanning the optical and IR were needed. Due to the all-sky nature of the Swift-BAT sample, data from various surveys were collected.

To obtain counterpart photometry in the Near and Mid Infra-red (NIR and MIR) for as many of our observed AGN as possible, we chose the data sets of the Wide-field Infra-red Survey Explorer (WISE)[4] and 2 micron all sky survey (2MASS)[5]. We compiled MIR photometry from the online database of the $WISE$ mission, served on the NASA/IPAC website, spanning four bands at 3.5, 4.6, 12 & 22 μm. Since our targets are well-resolved nearby galaxies, we used the GMAG photometric measurements in all cases. These are photometry using apertures scaled to the 2MASS Extended Source Catalog (XSC) size measurements, with a correction for the PSF of the WISE images. We converted WISE magnitudes to fluxes using the standard conversions from the online WISE Explanatory Supplement. The all-sky 2MASS XSC provides photometry in 3 NIR bands (J, H, K_s) for all the BAT AGN. We used the isophotal curve-of-growth magnitudes in this work, and employ standard conversions from 2MASS magnitudes to fluxes from the online 2MASS Explanatory Supplement.

To provide better constraints on the star forming component of each AGN (as explained

---

[4] `https://www.nasa.gov/mission_pages/WISE/main/index.html`

[5] `https://www.ipac.caltech.edu/2mass/`

in Section 4.1), Far Infra-red (FIR) photometric data was added. We obtained *Herschel* photometry for the BAT AGN from the data release described in Shimizu et al. (2017), based on the analysis presented in Meléndez et al. (2014) (PACS) and Shimizu et al. (2016) (SPIRE). We used their best measurements for the integrated photometry of the sources, covering 5 bands: PACS 70 & 160 μm and SPIRE 250, 350 & 500 μm.

Currently, there is no all-sky optical photometric survey, making the collection of optical photometric points for the full BAT AGN sample a more complex process than for the IR. In order to obtain the highest quality photometry possible for our SED fitting, we prioritised the following order of surveys: The Carnegie-Irvine galaxy survey[6], the HyperLEDA extragalactic survey[7], the NASA sloan atlas archive[8], SDSS[9], Pan-STARRs[10] and finally RC3 from the NASA Extragalactic Database (NED)[11].

The NASA Extragalactic Database (NED) supplies a heterogeneous dataset of photometry from the literature. We obtained B band photographic photometry of a subset of galaxies from the NED version of the RC3 catalog (de Vaucouleurs (1991), Corwin et al. (1994)). The SDSS and PanSTARRS optical imaging surveys yielded magnitudes in 6 bands from u–y. From the photometric catalogs of these surveys, we used the CMODEL magnitudes, which combine two different light profile models of extended sources to produce best-effort integrated photometric measurements. Where possible, we replace the SDSS database magnitudes with those from the NASA Sloan Atlas (NSA), a value-added resource for nearby galaxies with more accurate photometry for extended sources. We also used, where available, HyperLEDA measurements in five bands (UBVRI) which are homogenised curve-of-growth photometry as presented in Prugniel and Heraudeau (1998). Finally, for a small number of galaxies, curve-of-growth galaxy photometry in the BVRI bands is available from Carnegie-Irvine Galaxy survey (CGS; Ho et al. (2011)).

---

[6] `https://cgs.obs.carnegiescience.edu/CGS/Home.html`

[7] `http://leda.univ-lyon1.fr/`

[8] `http://www.nsatlas.org/`

[9] `https://www.sdss.org/`

[10] `https://panstarrs.stsci.edu/`

[11] `https://ned.ipac.caltech.edu/`

Chapter 3

Simulations

In this section we will introduce the simulations used in this project. We will firstly outline the simulation calibration, sub-grid physics employed and some results from previous studies. We will then describe details specific to this project such as the initial constraints used to attain the parent data set and the calculation of some of the relevant properties. The processes for the comparison sample are given in Section 4.2.

3.1 EAGLE

Most successful cosmological simulations require AGN feedback in order to reproduce some of the properties of the observed universe (Bower et al. (2006), Croton et al. (2006)). Two of the most popular types of simulations are semi-analytic models (SAMs) (e.g Lacey et al. (2016)) and Hydrodynamical simulations (e.g Crain et al. (2015), Schaye et al. (2015)). Within this project, we concentrate on the latter.

The Evolution and Assembly of GaLaxies and their Environments (EAGLE) is a suite of hydrodynamical simulations [1]. The simulations use an enhanced version of the GADGET-3 Smoothed Particle Hydrodynamics (SPH) code (Springel (2005)). This includes a modified hydrodynamics equation solver, time-step limiter ($\Delta t \approx 1$ Myr) and treats baryonic processes with sub-grid physics. The cosmological parameters EAGLE uses are those from the Planck mission (Planck Collaboration et al. (2015)), where $\Omega_\Lambda = 0.693$, $\Omega_m = 0.307$, $\Omega_b = 0.04825$ and $H_0 = 67.77$ km s^{-1}. A fuller description of the exact specifications can be found in Schaye et al. (2015) and Crain et al. (2015).

---

[1] `http://icc.dur.ac.uk/Eagle/`

Due to limited computing power, simulations have a limited resolution. This constrains simulations to either work with very high resolution and small scales, obtaining very accurate data but with low sample statistics, or on larger scales with lower resolution, obtaining large sample statistics with less precise data. EAGLE is found in the latter catagory, a cosmological simulation. To account for all processes which cannot be resolved numerically (in EAGLE $\mathrm{m}_g < 1.81 \times 10^6$ $\mathrm{M}_\odot$ or $\mathrm{m}_{dm} < 9.70 \times 10^6$ $\mathrm{M}_\odot$) such as star formation or supernovae events sub-grid physics is employed (Crain et al., 2015). The ideology is to describe these processes as simply as possible and to depend only on the local hydrodynamic properties. Some of the processes included in the sub-grid prescription are stellar mass loss due to supernovae events or winds from AGB or massive stars, radiative cooling and heating and the Initial Mass Function (IMF).

As they relate most directly to our observations, star formation and black hole accretion are the most important of the sub-grid physical processes in EAGLE to consider. Star formation is modelled according to Schaye and Dalla Vecchia (2008). This law approximates star formation as a stochastic process, based on the pressure dependant Kennicutt-Schmidt law with a Chabrier (2003) IMF. In this law, if the gas particle density is greater than a pressure dependant critical density, then star formation can take place. Black holes are seeded in the densest gas particle in every dark matter halo greater than $10^{10}h^{-1}$ $\mathrm{M}_\odot$. The black holes then grow through accretion of other particles, i.e other particles which fall onto this black hole seed. Energy gained through this process is then modelled as an energy reservoir at each timestep. This energy reservoir is then given a probability of being injected back into the surrounding material thermally, assuming a radiative efficiency of $\epsilon = 0.1$ (i.e 90% mass-energy goes into the growth of the black hole and the other 10% is radiated). The exact contributions of all of the sub-grid processes are then calibrated. The calibration of the models is based on the galaxy stellar mass function, the black hole mass - bulge mass relation and galaxy size - stellar mass relation at $z = 0.1$ (Crain et al. (2015)).

EAGLE has, however, also been shown to reproduce many present day observations to good agreement without specific calibration, such as galaxy colours, the Tully-Fisher relation, the evolution of the cosmic star formation rate, the passive galaxy fraction, rotation curves and metallicities to name a few (Schaller et al. (2015), Lagos et al. (2015), Trayford et al. (2015), Furlong et al. (2015), Schaye et al. (2015)). Similar to these studies, our comparison should serve as an independent test of EAGLE as the simulations have not been calibrated specifically to reproduce the observables of interest in this project, namely the star formation properties of AGN.

EAGLE also has various models which can include different sizes of the cosmological simulations (or box sizes), resolutions of the particles or physical models (e.g AGN feedback or not). Further details of these variations can be found on the EAGLE database or in McAlpine et al. (2016). The standard model referred to hereafter, incorporates AGN feedback and standard values for factors such as viscosity, hydrogen column densities etc. which can be found in Crain et al. (2015). These factors need to be accounted for carefully when making a comparison to the local universe as either the behaviour or the amount of extreme objects can vary. This phenomenon can be seen in Figure 3.1 where, going from left to right, when we increase the box size, we observe greater numbers of more luminous or higher star forming objects. The greater the volume of our sample or box, the more statistically probable it is to observe more extreme objects.

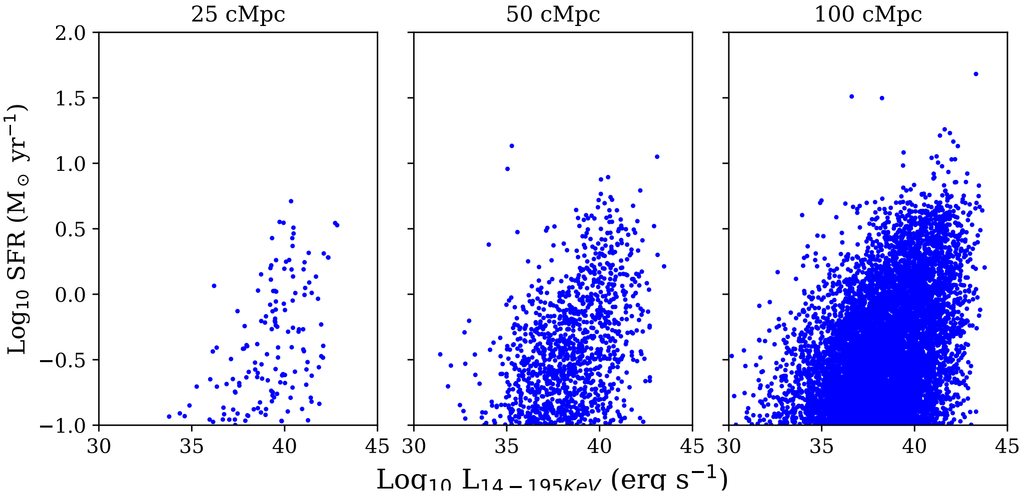

Figure 3.1: Here we see the standard EAGLE reference model (AGN feedback included) in three different box sizes (sizes given overhead). We plot the SFR versus X-ray luminosity, to see how many extreme objects we obtain in each box size.

3.2 Simulated Comparison Sample

The volume of the full BAT AGN sample ($z < 0.05$) is significantly larger than the volume of the largest EAGLE simulations ($\sim$ 40 times bigger). To be able to negate volume driven effects as much as possible, we use the biggest box size of 100 cMpc^3. We also use the standard EAGLE reference model which applies AGN feedback.

To access the properties of galaxies within EAGLE we queried the public database using the SQL interface. A full description of the exact querying process can be found in McAlpine et al. (2016). Some properties in low mass haloes may be inaccurate due to the statistical effect of containing low amounts of particles (e.g $N \lesssim 100$), hence a stellar mass cut of $M_* > 10^8 M_\odot$ was employed. To standardise the measurements of properties such as SFR or BHAR across the simulated galaxy sample we also used the recommended aperture of 30 kpc (McAlpine et al. (2016)).

Most observables such as the stellar mass, black hole mass, SFR and halo masses are directly available from the database. To calculate the X-ray luminosity, we took the BHAR given by the database and converted the value into bolometric luminosity using $L_{BOL} = \epsilon \times \dot{m}c^2$, assuming a radiative efficiency of $\epsilon = 0.1$. We then assumed that 10% of the radiated energy is in the X-ray regime (McAlpine et al. (2017)). EAGLE also produces the shape of the cosmic evolution of the average SFR well, however Furlong et al. (2015) found that EAGLE predicts a $\simeq 0.2$ dex lower $\log_{10}$ SFR over all epochs. Therefore, as advised in McAlpine et al. (2017), we also applied a +0.2 dex offset to all our SFRs.

Altogether the database yielded 29737 galaxies above a stellar mass of $M_* > 10^8 M_\odot$. Most of these objects, however, are inactive galaxies or AGN that would be too faint to be detected by Swift-BAT. The exact process of the matching of the simulated comparison sample (EAGLE AGN) to our final Swift-BAT AGN sample (or BAT AGN) can be found in Section 4.2. As a summary, of these 29737 objects, 134 AGN were chosen as our EAGLE comparison sample (EAGLE AGN).

Chapter 4

Methods

In this section we will describe the methods used throughout this project. This will firstly cover the SED fitting procedure to estimate the SFRs and stellar masses. Next we will describe the volume and flux matching procedure needed to account for biases in both the observational and simulated samples. Then we will describe the use of the merger trees system in EAGLE used to track the average evolution of two differently selected populations of AGN. This will be followed by the techniques used in the high time resolution data to observe how quasar-like events have an effect on the host galaxy star formation within EAGLE and finally we will describe the Bayesian fitting routine used in parts of this project.

4.1 SED Fitting of the BAT AGN using Fortes Fit

SFRs can be estimated using various techniques. Conversions from Hα, UV light and radio emission are a few (see Kennicutt and Evans (2012) for a summary). A lot of the estimates from these methods, however, can be significantly contaminated by emission from the AGN itself. The UV can be dominated by emission from the accretion disk itself, where it peaks in luminosity. This is especially prominent for unobscured AGN, where the observer has an almost direct view of the central component of the AGN. Estimations of the SFR in the radio can be contaminated by non-thermal radiative processes such as synchrotron radiation emitted from relativistic jets and/or the central regions.

Star formation, however, also emits strongly in the IR at various wavelengths. This is due to the absorption and re-emission of UV or optical light from young stars via the dust rich clouds that typically surround star forming regions. Similarly, the AGN dusty torus also emits in the IR, however due to the proximity of the torus to the AGN the temperature of the dust is higher than that of the dust around star forming regions (See Netzer et al. (2007) and references herein). Therefore the emission peaks in the MIR, dropping off sharply as we reach the FIR, where re-emitted light from star formation dominates (Rosario et al. (2012)).

In order to estimate SFRs and the stellar masses we use SED fitting on the photometry described in Section 2.2. We use the FortesFit[1] fitting routine for this task. FortesFit is a python based fully Bayesian fitting routine. It contains a library of parameterised model SEDs that work additively in order to try and fit the full SED to the data points provided. We firstly input the *priors* of certain parameters, such as the AGN type classification in order to better constrain the expected contribution of various components, minimising the chance of mis-fitting. The fitting routine then runs, providing *posterior* probability distributions for various values such as the AGN luminosity component, stellar mass and star forming luminosity in the IR. Example SED fits can be found in Appendix A.

To convert the total integrated luminosity component due to star formation into the SFR, we use equation 4.1 below, taken from Kennicutt and Evans (2012).

$$Log_{10}(SFR) = Log_{10}(L_{IR,SF}) - 43.41 \tag{4.1}$$

A basic test of the reliability of our SED fitting is to plot the AGN X-ray luminosity versus the total integrated IR luminosity component from the AGN estimated by the SED fits. This is shown in Figure 4.1. The black points with error bars are sources with reliable estimates ($> 3\sigma$) with errors derived from the 16^{th} and 84^{th} percentiles on the posterior distributions. The red crosses show upper limits ($< 3\sigma$), where there are not enough photometry points or photometric upper limits used to estimate the IR component of the SED to a high enough accuracy. The blue line with shading represents the best fitting line with 95% confidence limits as given by the Linmix bayesian linear regression algorithm, explained in Section 4.5. As seen, there is a fairly good fit with relatively little scatter, indicating that the SED fitting has worked well. Equation 4.2 shows the formula of the best fitting line with associated errors calculated from the standard deviation, where $L_{IR,AGN}$ is the IR luminosity associated with the AGN component, and $L_{14-195KeV}$ is the hard X-ray luminosity.

$$Log_{10}(L_{IR,AGN}) = (0.78 \pm 0.08)Log_{10}(L_{14-195KeV}) + (9 \pm 3) \tag{4.2}$$

---

[1] `https://github.com/vikalibrate/FortesFit`

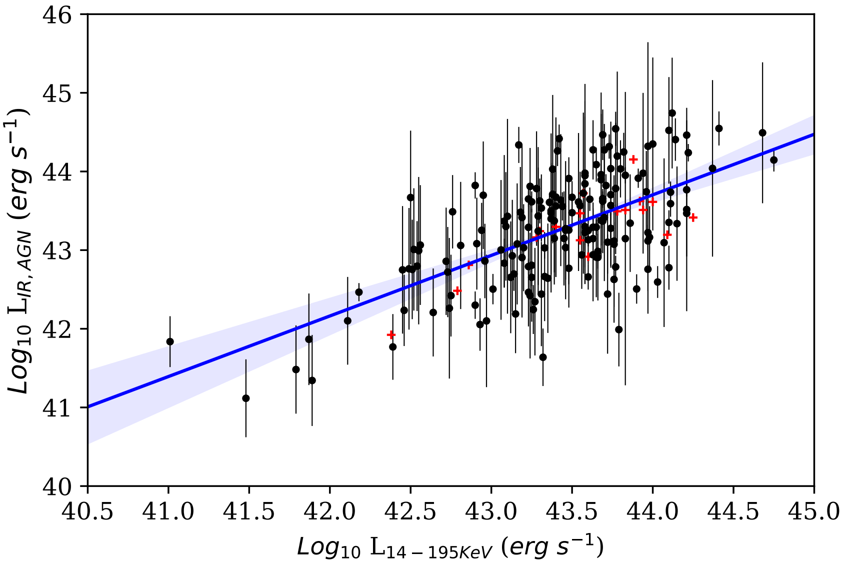

Figure 4.1: The integrated IR luminosity component from the AGN versus the X-ray luminosity. Black points represent estimations of the SFR with error bars derived from the 16^{th} and 84^{th} percentiles on the posterior distribution. Red crosses are 3σ upper limits. The blue line represents the median best fit line as determined by the Linmix bayesian linear regression code with the shaded areas representing the 95% confidence limits.

4.2 Flux and Volume Matching the Samples

We have already outlined that volume effects can play a significant role when selecting two samples to compare, however instrument sensitivity can also bias results when comparing observations to simulations. An initial comparison of the luminosity and SFR distributions between the full BAT sample and a sample of AGN in EAGLE selected using a luminosity cut ($L_{14-195KeV} > 10^{41}$ erg s^{-1}) indicated a poor agreement (Appendix B.1 and Appendix B.2). This, however, was due to the disparities outlined earlier between the two samples. Due to the flux sensitivity of the Swift-BAT instrument our full BAT sample is biased towards higher luminosity AGN. The larger volume ($\simeq$ 40 times greater than that of the EAGLE simulation box) means the statistical chances of encoutering high SFR objects is also higher. To account for the volume effects we firstly applied a redshift upper bound of $z = 0.1556$ on the full BAT AGN sample in order to exactly match the volumes of the observed and simulated sample. This reduced our observational sample to 72 AGN, hereafter our BAT AGN sample.

To account for the statictical bias shown in EAGLE towards lower luminosity objects, we also carried out flux matching. In order to mimic the sensitivity of the Swift-BAT instrument, we used a random number generator to assign a flux limit according to the instrument's sensitivity to every object in EAGLE. This is 1.1×10^{-11} erg sec^{-1} cm^2 for 50% of the observed sky, 1.48 × 10^{-11} erg $\sec^{-1}$ cm^2 for 40% and 1.7 × 10^{-11} erg $\sec^{-1}$ cm^2 for the remaining 10%.

To compute the expected X-ray fluxes of AGN in EAGLE, we employed the cartesian coordinate system to calculate the distances from each galaxy to the central point of the simulation box (i.e x, y, z = 50 Mpc). We then used these in conjunction with the calculated X-ray luminosities in order to find the expected flux. If the expected X-ray flux was above the assigned flux limit, then the object was used in the comparison sample. If the value was below the limit, the object was discarded. This then reduced the amount of low luminosity objects which were yielded compared to a simple luminosity cut. These objects are usually lower in star formation rate and hence introduce a bias into our results. The results of this process can be seen in Figure 4.2. The left panel shows the distribution in $\mathrm{L}_{14-195KeV}$ and z in both our BAT AGN and all EAGLE galaxies before the flux matching and the right panel shows our BAT AGN and EAGLE galaxies which were above the flux limit. This left a final simulation comparison sample of 134 objects, slightly more than, however still fairly similar, to our BAT AGN. The slight difference in numbers is to be expected as some AGN in the local universe may be obscured enough to remain un-detected by Swift-BAT. This defines our EAGLE AGN comparison sample (Hereafter EAGLE AGN).

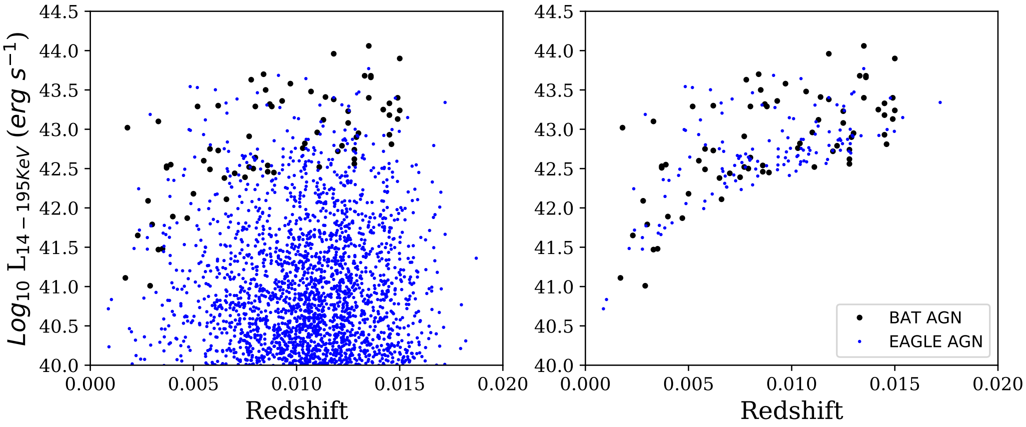

Figure 4.2: The left hand panel shows the distribution in redshift and X-ray luminosity for each galaxy (blue points) in EAGLE from an observer at the centre of the box. These are compared to the BAT AGN data (black points). The right hand panel shows this distribution once the flux mask is applied. The sensitivity of Swift-BAT instrument is well replicated by this flux matching process.

In order to investigate how well EAGLE reproduces the star forming properties of the local AGN universe, and how well it reproduces other host galaxy properties, we directly compared our BAT AGN and EAGLE AGN samples. The key tests were EAGLE's predictions of SFR and X-ray luminosity distributions, any major disagreement would indicate a problem with either EAGLE's predictions or our observations.

To investigate how well EAGLE agrees with the observed universe Scholtz et al. (2018) compared the sSFR distributions of their observed AGN and EAGLE AGN comparison samples. They also compared the position of these two AGN samples in sSFR vs stellar mass to the sSFR main sequence from Schreiber et al. (2015) and the entire population of galaxies (both AGN and not) in EAGLE. If AGN feedback quenches star formation, then we should expect our AGN samples to lie below the sSFR main sequence. Therefore we also performed this comparison in Section 5.4.

4.3 Use of the Merger Trees within EAGLE

When observing a sample of galaxies, we only see a small snapshot of its entire lifetime. Though various techniques such as looking for similar galaxies at high redshift, stellar population models, spectroscopy etc. we can attempt to infer the general history of a specific type of galaxy or galaxy itself, however there are limitations to each method. One advantage of simulations is that each galaxy and its properties can be followed from high redshift to the present day. By using this technique, we looked at the host galaxy evolution of AGN selected at the present day to those at higher redshift to compare the relative evolutionary paths.

The individual histories of galaxies in EAGLE can be traced over 28 snapshots from $z = 0$ to $z = 20$ using the merger tree system. To discover the entire assembly history of a galaxy at $z = 0$, the paths between the present day galaxy and all of its original descendants can be traced, creating an entire tree. Alternatively, to simplify the evolutionary history, the main branch of the galaxy can be traced from the present day galaxy to the galaxy with the TopLeafID, i.e the path of the most massive progenitor at each time point. An example of a merger tree can be seen below in Figure 4.3.

To track the histories of an AGN population within EAGLE (selected at $z = 0$) without overcomplications, we chose to track the main branch of each galaxy. Although a major merger may greatly affect the galaxy properties in a single galaxy between any two snapshots, the simulation merger rate is relatively low. This means that when we observe the average host galaxy properties of an entire AGN sample, the effects of any one AGN undergoing a major merger between two snapshots is washed out.

We took an AGN sample within EAGLE using a luminosity cut of $L_{14-195KeV} > 10^{42}$ erg

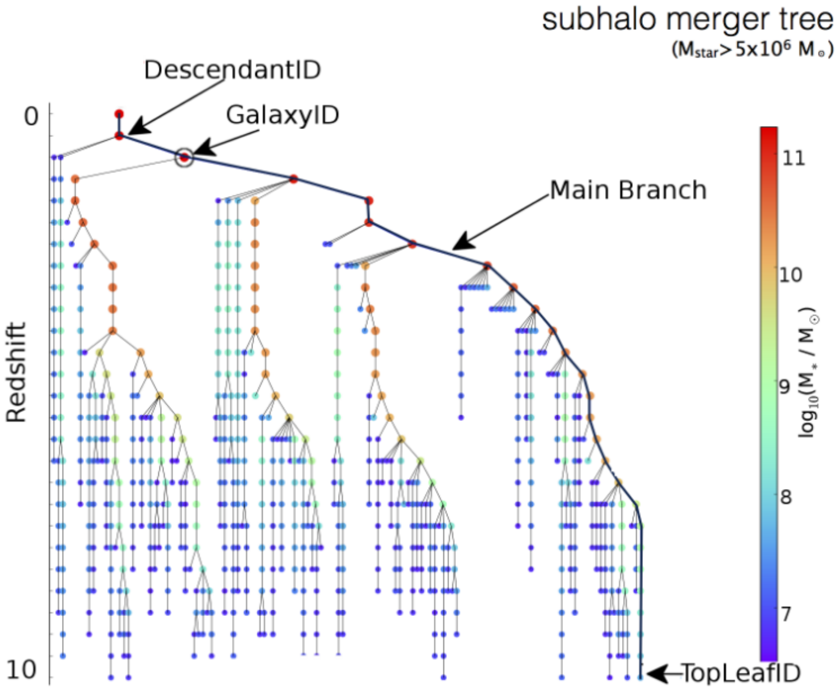

Figure 4.3: Taken from McAlpine et al. (2016). This shows the individual merger tree of a galaxy within EAGLE. The main branch between the present day galaxy and TopLeafID is given in black. All of the other descendants can be seen on the other branches of the merger tree.

s^{-1} at $z = 0$, yielding 274 AGN. Although not an exact match to our EAGLE AGN sample outlined in Section 4.2, the overlap is substantial and allows us to observe a larger sample size, reducing statistical biases. To compare the evolution of two differently selected populations, we also followed the main branches of the comparison sample used in Scholtz et al. (2018). Their EAGLE AGN sample was selected to have a stellar mass $M_* > 10^{10}$ $M_\odot$, an X-ray luminosity Lx $> 10^{43}$ - 10^{45} and a redshift range of $1.4 < z < 3.6$, yielding 290 AGN. Surprisingly, 50 AGN were found to be contained in both samples (18% of the Scholtz AGN (selected at z $\sim$ 2) and 17% of AGN selected at $z = 0$).

To allow the Scholtz et al. (2018) AGN sample to be tracked back far enough in cosmic time before they were selected we tracked the histories from the present day to redshift $z = 5$. To observe the cosmic evolution of the most important host galaxy properties, the SFR, stellar mass and black hole mass were queried at each snapshot. In order to observe the average host galaxy properties at each snapshot, the median values were calculated. Finally, to investigate if and under what conditions AGN feedback plays a role in quenching star formation within EAGLE, we also compared our AGN sample and those of Scholtz et al.

(2018) to their respective Schreiber et al. (2015) star forming main sequences.

4.4 High Time Resolution Data in EAGLE

It is also possible to track galaxies within EAGLE at a much higher time resolution than the 28 snapshots between $z = 0$ and $z = 20$ given on the database. In order to investigate in detail the processes driving the quenching of star formation in EAGLE, we used high time resolution snapshots (or 'snipshots'). The SFR, BHAR, stellar mass and black hole mass were calculated for every 1 Myr snipshot for each galaxy within EAGLE above a stellar mass of 10^9 $M_\odot$ at $z = 0$. The evolution in these host galaxy properties could then be tracked by combining all the snipshots for one individual galaxy into a timeline.

In order to observe the events which have the highest likelihood of impacting on the star formation of the host galaxy and to avoid any significant redshift evolution in the BHAR and SFR, we only considered those galaxies which underwent a quasar-like phase, ($L_{BOL} > 10^{45}$ erg s^{-1}) at some point within the last 700 Myr (or $z < 0.05$). We found 89 objects which fulfilled these criteria from $\simeq$ 13000 galaxies in the original data set, 14 of which are also in our EAGLE AGN sample. An example of a snipshot timeline for one of these galaxies can be found below in Figure 4.4.

The quasar-like event is the most powerful event in the galaxies timelines and should in theory deliver the most feedback to the host galaxy. In order to find out how these large amounts of feedback in EAGLE may affect the star formation of a general population of galaxies, we set the peak (highest) accretion event for each of the 89 galaxies to $t = 0$. The timeline for each individual object was then extended either side of this event, i.e the whole timeline was shifted. The average behaviour these events have on the entire sample was then found by stacking each of the 89 galaxies and calculating the median and the 14^{th} and 86^{th} percentiles for the BHAR and sSFR at each time step. As the peak accretion event occurs at a different time point in each snipshot, this means that the amount of time steps before and after each peak accretion is different, hence the stacked sample spans $\approx$ 1400 Myr. This has the effect that at different time steps, there are different amounts of AGN contributing to the stacked behaviour at $t = 0$, all 89 objects contribute to the sample, however at $t = \pm 350$ this expected to be approximately half. To avoid the biases introduced by low sample statistics, we use the first/last 200 Myr of the stacked timelines but are careful of overinterpreting what they show.

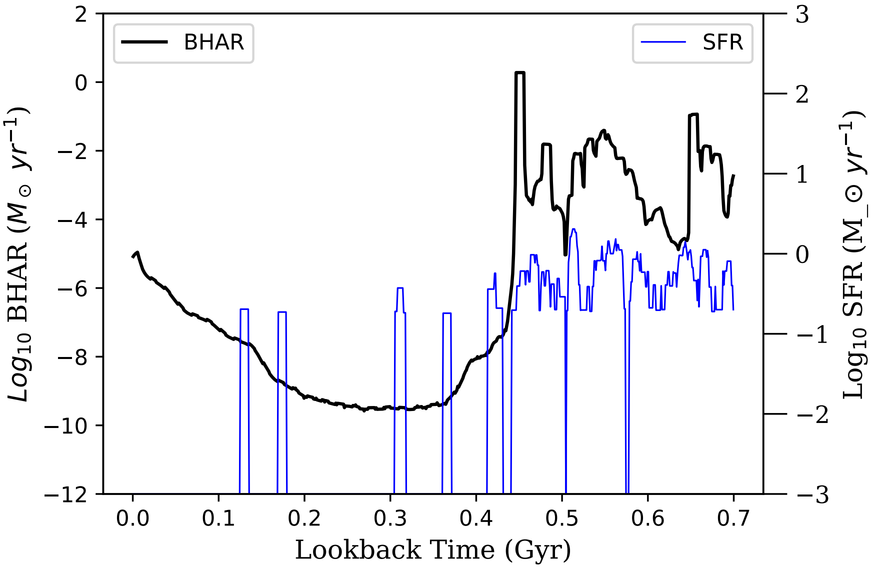

Figure 4.4: An example of one of the snipshots. The BHAR rate is outlined in black, and the SFR in blue. The x-axis outlines the lookback time, i.e 0 represents the 'present day'. Noticible is that the BHAR and SFR are on average higher until the peak black hole accretion event at $t \approx 0.45$. Afterwards the BHAR drops significantly ($\sim$ 7 orders of magnitude) and the star formation is suppressed with the exception of a few bursts driven by the stochastic prescription assigned to star formation.

4.5 Linmix Bayesian Fitting Routine

In order to reveal any trends in our data between two variables, such as SFR and X-ray luminosity, we needed a fitting model that accounted for errors and non-detections. Linmix is the Bayesian linear regression fitting code originally written in IDL for astronomers. In their paper, Kelly (2007) showed that the code outperformed other similar fitting codes. It accounts for both errors in the dependant and independent variable as well as integrating upper limits into it's calculations. This ability to account for upper limits made it ideal for our project. A python version was created and is publicly available on Github[2], where we obtained our version. A fuller description of the mathematics and implementation can be found in Kelly (2007) or on the github page, however we will outline in short the basis of this code.

Bayesian linear regression relies on probability distributions in both the slope and intercept in order to calculate their values. It takes a *prior* belief or *distribution* of the two (i.e the slope and intercept for a given amount of data points) and updates this to a *posterior* belief

---

[2] `https://github.com/jmeyers314/linmix`

when a new data point or event is added. This updated belief for the value of the slope and intercept is calculated according to Bayesian statistics. Once updated, this process is repeated until the solutions reach a minimal point of converge; i.e the difference between the prior and posterior is smaller than a critical value. The modelling of each posterior distribution, however, cannot always be done analytically and hence numerical Monte-Carlo methods must be used to solve the integrals describing the distribution.

Kelly (2007) uses a version of the Markov-Chain Monte-Carlo methods in order to numerically solve the integrals in order to update the posterior. An extra term is also used in order to account for upper limits separate to the main data.

From these processes, a distribution of the posterior values for alpha and beta (the intercept and the slope respectively) can be assembled. The best fitting line can then be found from the medians of the two distributions, the error calculated from the standard deviation of the sample and the 95% error values from the appropriate percentiles.

Chapter 5

Results

In this section we present the results from our analyses. We will initially present the trends in our full BAT AGN sample. This will be followed by the results of our comparison of the star formation properties of the BAT AGN and EAGLE AGN samples. We will then present our comparison of the average evolution of host galaxy properties from two differently selected AGN samples in EAGLE. Finally we will present the effect that quasar-like accretion events have on their host galaxies within EAGLE.

5.1 Trends in the Full Swift-BAT AGN Sample

In Section 4.1, we plotted the X-ray luminosity versus the IR luminosity from the AGN component in order to check that our SED fitting was consistent. A negative or flat trend would have indicated that our SED fitting may have encountered problems. Similarly in order to check that the SFR estimates for the full BAT AGN sample obtained from our SED fitting were also consistent and within the ranges expected (SFRs on the order 1000 $M_\odot$ yr^{-1} or more would indicate most likely that the SED estimations were wrong), we plot the SFR versus X-ray luminosity ($L_{14-195KeV}$) in Figure 5.1. We then compare the resulting SFRs and trends in the data to previous studies. To find the best fitting line and associated error, and thereby the trends in the data, we ran the Linmix Bayesian linear regression code described in Section 4.5. As we can see there is little correlation found between the two variables in our data, as shown by the relatively flat best fit line. The median best fitting line recovers the following relationship between the SFR and the X-ray luminosity given in Equation 5.1. The narrow shaded confidence intervals indicate that we have a sharp probability function and therefore it is likely that little or no correlation exists.

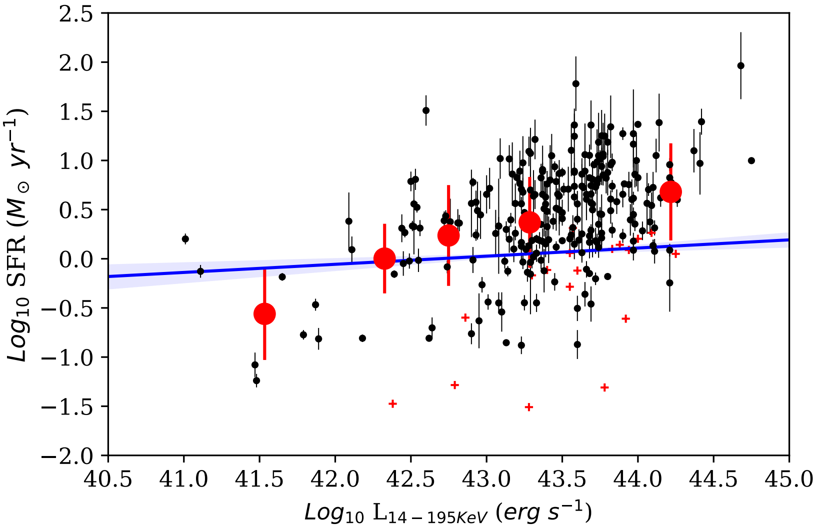

Figure 5.1: Star Formation Rate versus X-ray luminosity for the full Swift-BAT sample ($z < 0.05$). Black points with 1σ error bars show all sources with SFR measurements. Red crosses show SFR upper limits. The blue line shows the median best fitting from Linmix with associated error indicated by the shaded regions. Red points show the mean SFRs divided into X-ray luminosity bins. We see reasonable values expected for the SFRs $\sim 0.1 - 100$ $M_\odot$ yr^{-1} and the flat trend seen in previous studies between SFR as a function of X-ray luminosity. This means our estimations are fairly reliable.

$$Log_{10}(SFR) = (0.08 \pm 0.02)Log_{10}(L_{14-195KeV}) - (3 \pm 1) \tag{5.1}$$

We find that our flat relation between the average SFR and X-ray luminosity to be fairly consistent with what is expected from previous studies for mid-luminosity AGN (Rosario et al. (2012), Stanley et al. (2015), Shimizu et al. (2017)). To verify that our results also fit previously observed trends in the redshift evolution of the average SFR, we separated our sample into 5 equal bins of X-ray luminosity and plotted the mean integrated star forming IR luminosity versus the AGN bolometric luminosity (L$_{BOL}$ = 10 × $L_{14-195keV}$). We then compared our points to those in Stanley et al. (2015), as can be seen in Figure 5.2. Due to the amount of upper limits estimated on the star forming IR luminosity in Stanley et al. (2015), they use the Kaplan–Meier (K-M) product limit estimator to calculate a mean. In our study we have relatively few upper limits, so we calculate the simple mean of the sample. We see, despite the different methods, that our points are in good agreement with the redshift evolutionary trends of the average SFR found in Stanley et al. (2015). This means that AGN follow the same trends inactive galaxies do in their average cosmic evolution, whereby the average SFR decreases with redshift (Schreiber et al., 2015).

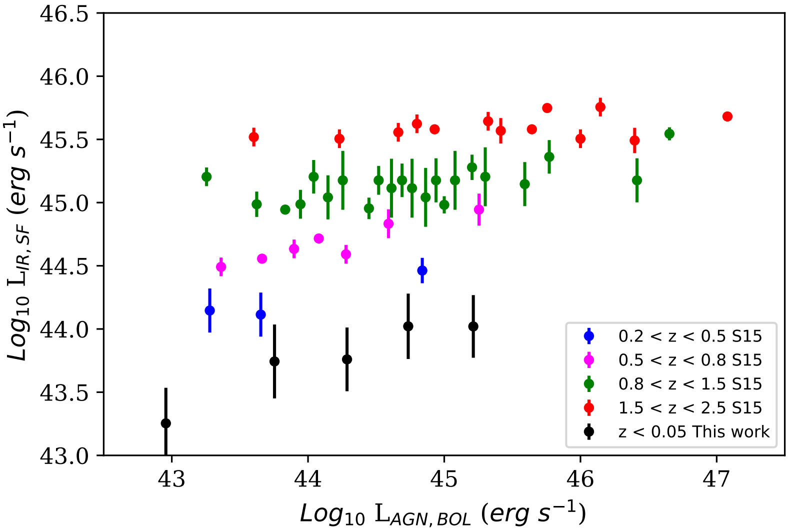

Figure 5.2: Comparison of our data (black dots) against the work of Stanley et al. (2015) (S15) (all other points). We see the expected decrease in average SFR with redshift as found by Stanley et al. (2015). The average cosmic SFR of star forming galaxies decreases with redshift from its peak at $z \sim 2$ to the present day. This shows that AGN follow similar behaviour to inactive galaxies.

5.2 Comparison of BAT AGN and EAGLE AGN

A key test of EAGLE is the reproduction of the observed SFR distributions, the X-ray luminosities and the expected fairly flat relationship of the BAT AGN sample (volume and flux matched) by the EAGLE AGN sample. If all of these factors are not reproduced well then we could conclude that EAGLE does not reflect the local AGN universe. This is shown in Figure 5.3.

On visual inspection we find good overall agreement between the two samples, with no distinct outliers as seen in the central panel of Figure 5.3. The $\log_{10}$ SFR distributions for the BAT AGN (EAGLE AGN) samples range from -1.47 to 1.51 $M_\odot$ yr^{-1} (-1.75 to 1.87 $M_\odot$ yr^{-1}) with a median value of 0.24 $M_\odot$ yr^{-1} (-0.01 $M_\odot$ yr^{-1}). In order to compare the shape and values of the distributions we ran an Anderson-Darling (A-D) test. The advantage of this method over a Kolomogorov-Smirnov or Chi-Squared test is that outliers are more heavily weighted, hence any extreme objects at each end of the distribution are accounted for more equally relative to those in the middle of the distribution. This allows for a fairer comparison. The statistic we recover from this test is a p-value of 0.20, in other words, a probability of 20% that our samples are drawn from the same parent sample.

We find that the $\log_{10}$ $L_{14-195keV}$ distributions for the BAT AGN (EAGLE AGN) range from

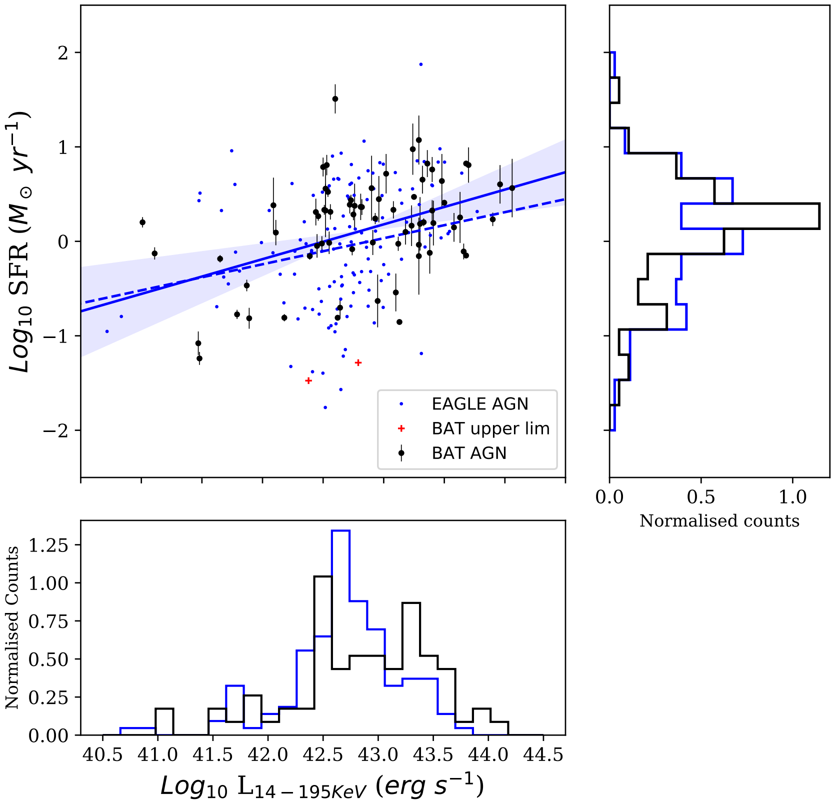

Figure 5.3: SFR versus X-ray luminosity for the volume and flux matched BAT AGN and EAGLE AGN samples. The solid blue line shows the median best fitting recovered from Linmix with the 95% confidence intervals in the shaded regions for the BAT AGN sample. The dashed line indicates the linmix best fitting for our EAGLE AGN sample. We see good agreement in the SFR distributions and a good replication by EAGLE of the expected fairly flat trend expected.

41.01 to 44.06 erg s^{-1} (40.72 to 43.77 erg s^{-1}) with a median value of 42.86 erg s^{-1} (42.71 erg s^{-1}). They have identical ranges, however the luminosities of the EAGLE AGN sample is on average lower. The p-value recovered from an A-D test is 0.018. Therefore it is unlikely that these two distributions are drawn from the same sample.

Comparing distributions is useful, however a comparison of the best fit trends found in the BAT AGN and predicted by the EAGLE AGN contain more information. The trend between the SFR and $L_{14-195keV}$ in the BAT AGN sample is given by Equation 5.2 and shown as the blue solid line in Figure 5.3. This differs from Equation 5.1 as we are using the BAT AGN sample (volume matched to $z < 0.01556$) rather than the full BAT AGN sample.

$$Log_{10}(SFR) = (0.36 \pm 0.10) Log_{10}(L_{14-195KeV}) - (15 \pm 4) \tag{5.2}$$

In comparison, running linmix on our EAGLE AGN sample, we recover Equation 5.3. This is shown as the blue dashed line in Figure 5.3. The EAGLE AGN sample is in good agreement with the BAT AGN sample, predicting the observed trend within error.

$$Log_{10}(SFR) = (0.28 \pm 0.10) Log_{10}(L_{14-195KeV}) - (12 \pm 4) \tag{5.3}$$

This shows that as well as reproducing to a significant degree the observational SFR distributions, EAGLE also reproduces the trends, within error, observed in the observational data between the X-ray luminosity and SFR. A similar SFR distribution with a different trend (e.g negative or highly positive) would have conflicted with previous observational evidence, indicating EAGLE could be wrongly predicting SFRs for individual galaxies.

5.3 SFR Distributions from Monte-Carlo Methods

Many AGN within EAGLE are missed by our flux matching technique which calculates the expected X-ray flux using the co-ordinates from the central point of the simulation box (see Section 4.2). These AGN may be as bright as those within our EAGLE AGN sample but are too far away from the centre of the simulation box for their flux to satisfy the flux limit applied to our selection of EAGLE AGN. These AGN may have lower or higher than average SFRs and hence may influence results. In order to check that an arbitrary point of the simulation is not biased, in this case the centre of the simulation box, we applied some Monte-Carlo (MC) style methods.

By assuming the distribution of galaxies in the local universe is approximately uniform we can model the amount of galaxies per redshift bin as a quadratic power law (example given in the left panel of Figure 5.4). This is not unreasonable as we expect only one significant cluster (Virgo) within the volume we are using, therefore this should not significantly bias our observational results. To do this, we used a random number generator based on a quadratic power law to assign a randomised redshift to each galaxy. Once the redshifts are assigned, assuming the same Planck cosmology applied to EAGLE, we can calculate the expected AGN X-ray flux from each galaxy. This allows us to repeat the same processes of flux matching described in Section 4.2 on the new X-ray flux values.

This technique allows us to randomly draw a different sample of lower luminosity AGN while retaining a large number of higher luminosity AGN which we would expect to see from most positions in the simulation box. We then ran an A-D test on the BAT AGN SFR distribution and the new EAGLE AGN SFR distribution in order to recover the p-value (or proxy for level of agreement). To utilise as many low luminosity AGN as possible, we ran this process of random assignment, calculation, flux matching and comparison 10,000 times, collecting the distribution of p-values observed in the right panel of Figure 5.4.

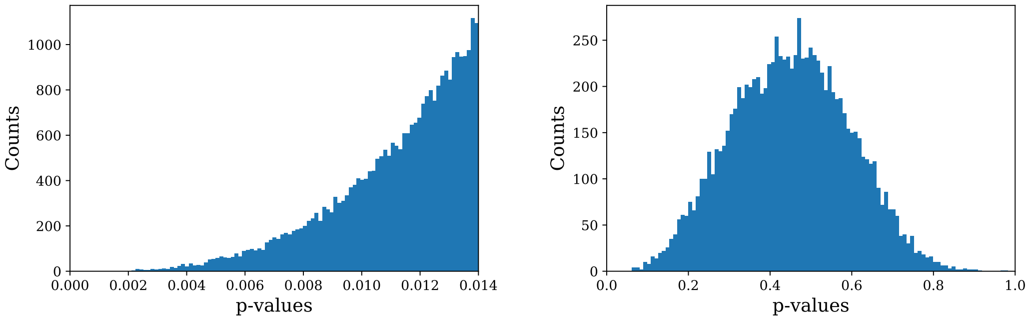

Figure 5.4: The left panel shows one set of the randomly generated distributions of redshifts assigned to all the galaxies in EAGLE, assuming a quadratic power law. Once the redshifts are assigned randomly to each galaxy, the same process of flux matching in Section 4.2 is carried out and the result from an A-D test of the two SFR distributions collected. The right panel shows the distribution of the p-values from repeating this process 10,000 times. The median p-value is 0.45, meaning on average, regardless of the viewer point in the box, there is a 45% chance that the SFR distributions stem from the same parent sample.

The median p-value of this distribution is 0.45, or a 45% chance of the BAT AGN SFR distribution and SFR distributions generated by the MC style methods coming from the same parent ditribution. The 16^{th} and 84^{th} percentiles have values of 0.30 (30%) and 0.60 (60%). This means the agreement in the SFR distributions found between the EAGLE AGN sample (measured from the central point of the box) and the BAT AGN sample is not just due to an arbitrary selection of "observing" point in the EAGLE simulations but is in general good agreement.

5.4 Comparison of sSFR distributions

Two samples may have similar SFR distributions, however if they have significantly different mass distributions, the comparison can be misleading. A comparison of the BAT AGN and EAGLE AGN sSFR distributions therefore should give a better indication of the level of agreement between these two samples than the SFR distributions alone. This is plotted below in Figure 5.5.

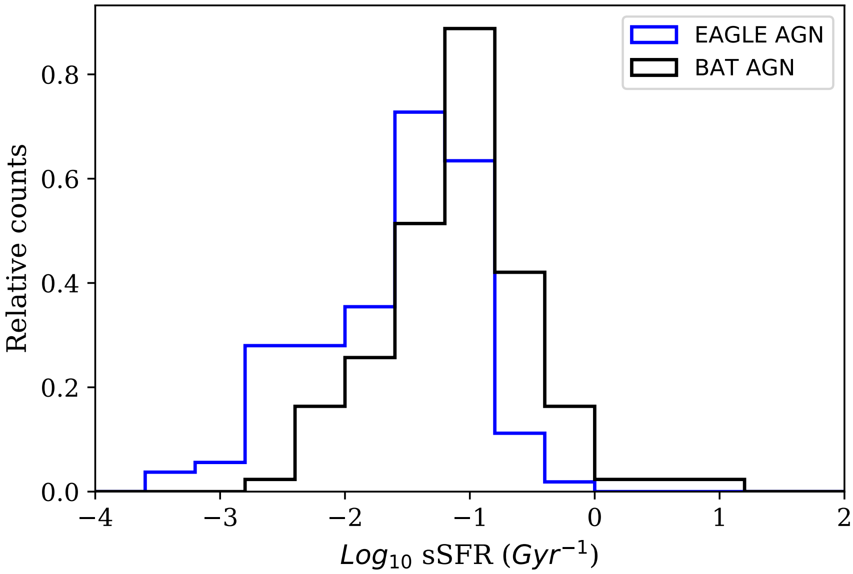

Figure 5.5: The sSFR distributions of the BAT AGN (black line) and EAGLE AGN (blue line). The shapes of the distributions are similar, with similar ranges, however the EAGLE AGN sSFRs are on average lower than those of the BAT AGN, leading to a mismatch of the two distributions.

The black line gives the sSFR distribution of the BAT AGN sample and the blue line the sSFR distribution of the EAGLE AGN sample. The median, 16^{th} and 84^{th} values of the BAT AGN (EAGLE AGN) sample are $-1.06^{-0.54}_{-1.69}$ ($-1.49^{-1.03}_{-2.38}$). The range is 3.61 (3.08). An A-D test gives a probability of $< 1\%$ agreement. The good level of agreement found between the SFR distributions of the BAT AGN and EAGLE AGN sample and the disagreement found in the sSFR indicates differences in the sSFR per stellar mass bin or conversely stellar mass per SFR bin. EAGLE on average predicts a population of slightly higher mass AGN (seen in Appendix C.1) and also slightly lower sSFR (seen in Figure 5.6).

To investigate the position of both the BAT AGN and EAGLE AGN samples relative to the sSFR main sequence, we split the BAT AGN sample into low and high stellar mass bins using the median stellar mass. We then took the median values of the sSFR distributions. For the EAGLE AGN sample and the average inactive galaxy population within EAGLE, we split the samples into 16 $\log_{10}$ stellar mass bins, each of 0.2 dex ranging from 8.9 - 12.1 and plotted the median. These results compared the sSFR main sequence as given in Schreiber et al. (2015) can be seen in Figure 5.6.

The red dotted line gives the sSFR main sequence as defined by Schreiber et al. (2015). The BAT AGN sample, (black points) lies below the main sequence by $\approx$ 0.2 and 0.3 dex

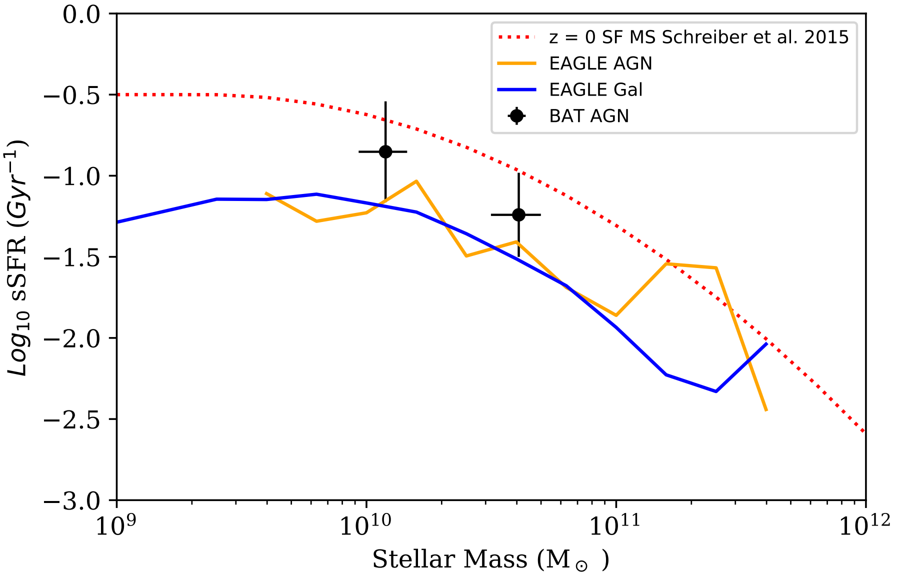

Figure 5.6: sSFR versus Stellar Mass for the BAT AGN sample (black points), EAGLE AGN (orange line), entire galaxy population in EAGLE (blue line) and the sSFR main sequence (red dotted line). The median of the BAT AGN lie below the sSFR main sequence but above the averge of all EAGLE galaxies, in agreement with the findings from Scholtz et al. (2018). The EAGLE AGN also lie below the sSFR main sequence, however at the same level as the average of all EAGLE galaxies, lower than expected. This indicates that EAGLE underpredicts the expected sSFRs of our BAT AGN.

respectively. The EAGLE AGN sample (orange line) lies ≈ 0.5 dex below the sSFR main sequence at most masses as does the inactive galaxy population (blue line). In their study, Scholtz et al. (2018) showed that both their observational and simulated AGN samples were in agreement with each other, lying below the sSFR main sequence, but above the average galaxy population. Our results with the exception of the EAGLE AGN sample display similar behaviour. This shows that the on average, the BAT AGN could be going through the process of having their star formation quenched, sitting below the main sequence, however are not fully quenched as they lie above the average of all galaxies which is dominated by red quiescent galaxies. The average EAGLE AGN also lies below the sSFR main sequence, indicating the quenching of star formation. The feedback employed by EAGLE is stronger than the precriptions employed by other simulations. This aggresive feedback could account for the difference seen between the EAGLE AGN and BAT AGN, however the exact cause of these differences will need to be investigated in further work.

5.5 The Evolution of AGN Host Galaxy Properties in EAGLE

When observing AGN, we only see a small window in its entire lifetime. Our theories about the evolution of AGN activity and their host galaxies therefore are built upon multiple observations of various objects, which may not necessarily follow the same evolutionary paths. Using simulation merger trees we can overcome this problem and follow an AGN across its lifetime. We must, however, be careful of over interpretation of the results. In order to explore if AGN selected at different epochs in EAGLE show the same behaviour over their lifetimes, we compare the average cosmic evolution of both samples.

In section 5.4, we outlined that the median of the EAGLE AGN sample from this work and the mode of that of Scholtz et al. (2018) lie below the star forming main sequence. To investigate the point at which the star formation starts quenching in EAGLE, we plotted the median SFR of our EAGLE AGN sample selected at $z = 0$ by a luminosity cut of $L_{14-195keV} > 10^{42}$ erg s^{-1} (hereafter Lx AGN) and the EAGLE AGN sample from Scholtz et al. (2018) (hereafter Scholtz AGN) in 20 snapshots ranging from $z = 5$ to $z = 0$. We then compared the two samples to their respective SFR main sequences. The respective main sequences were calculated from Schreiber et al. (2015) using the median masses and redshifts at each snapshot for both samples. The results are shown in Figure 5.7.

We observe that the Lx AGN sample follows approximately the mass matched SFR main sequence until $z \sim 1.5 - 2$. At this point the average SFR decreases relative to its main sequence. By $z = 0.62$ the difference in the SFRs is 0.44 dex, this relative decrease however remains fairly constant hereafter, as by $z = 0$ we see a difference of 0.50 dex. Similar behaviour is observed in the Scholtz AGN sample. The AGN galaxies approximately follow their SFR main sequence until decreasing relative to the main sequence at $z \sim 2.5 - 3$. By $z = 1.25$ we find a difference in the SFRs of 0.56 dex. This remains fairly constant as at $z = 0.1$ this difference is 0.62 dex. This could mean that the AGN feedback is most effective at a certain epoch when the galaxy reaches a critical mass as explained below. The galaxy, however, is still small enough to be majorly affected by AGN feedback with star formation therefore quenching and dropping relative to the main seuqunce. The galaxy would still grow at this point although more slowly, eventually assembling enough mass that the AGN feedback could play a more regulatory role rather than active quenching. This could account for the drop relative to the main sequence which is followed by a constant difference, however, would need to be investigated further.

In order to further investigate if the behaviour of these two differently selected AGN samples

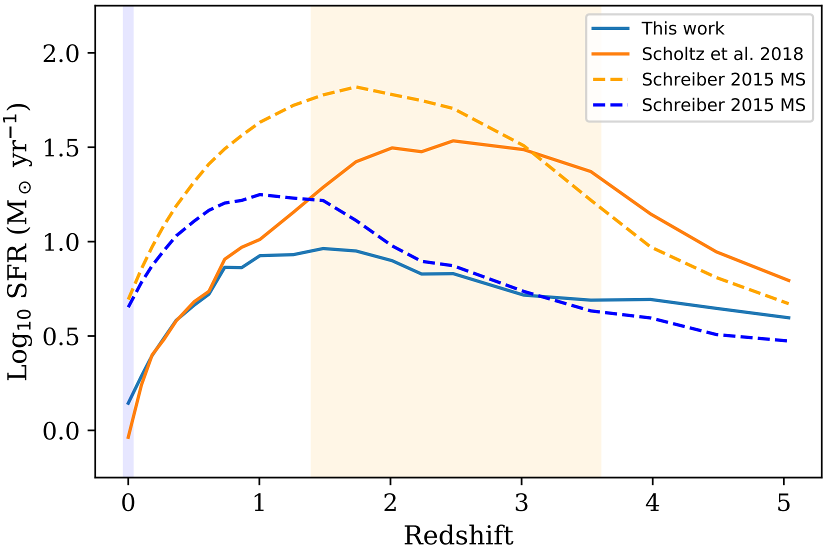

Figure 5.7: The evolution from $z = 5$ to $z = 0$ of an EAGLE AGN sample selected at $z = 0$ in this project (blue) and the EAGLE AGN from Scholtz et al. (2018) (orange). The dotted lines represent the respective star forming main sequences for each sample as perscribed by Schreiber et al. (2015). The shaded areas show the respective redshift selection epochs of the two samples. We see that the median SFRs follow approximately the respective main sequences for both samples before dropping below the main sequence. This is most likely due to AGN feedback.

is consistent with each other and to observe the average conditions under which the quenching of star formation may occur within EAGLE, we plot other AGN host galaxy properties as a function of redshift. Scholtz et al. (2018) showed that the broadening of sSFR distributions occurred at a critical stellar mass. Similarly Bower et al. (2017) showed that once a galaxy reaches a certain mass or gravitational potential within EAGLE, supernovae feedback is no longer effecient enough to eject gas from the galaxy, causing AGN activity to start as the SMBH has a gas supply. For these reasons we may expect the stellar mass or the black hole mass/black hole growth to play an important role. The rate of black hole growth also indicates the rate of energy being injected back into the host galaxy and so we may expect this feedback to quench star formation in the host galaxy. Finally, the sSFR provides a better indicator of any differences than the SFR alone. We therefore plot all of these host galaxy properties as a function of redshift in Figure 5.8 for comparison.

We can see in the top two panels of Figure 5.8 that AGN from the Scholtz AGN sample on average go through their greatest rate of stellar and black hole mass growth in an earlier epoch than the AGN in the Lx AGN sample. This difference is most noticeable in the bottom left panel where we have plotted the log of the black hole mass over the stellar mass, a proxy

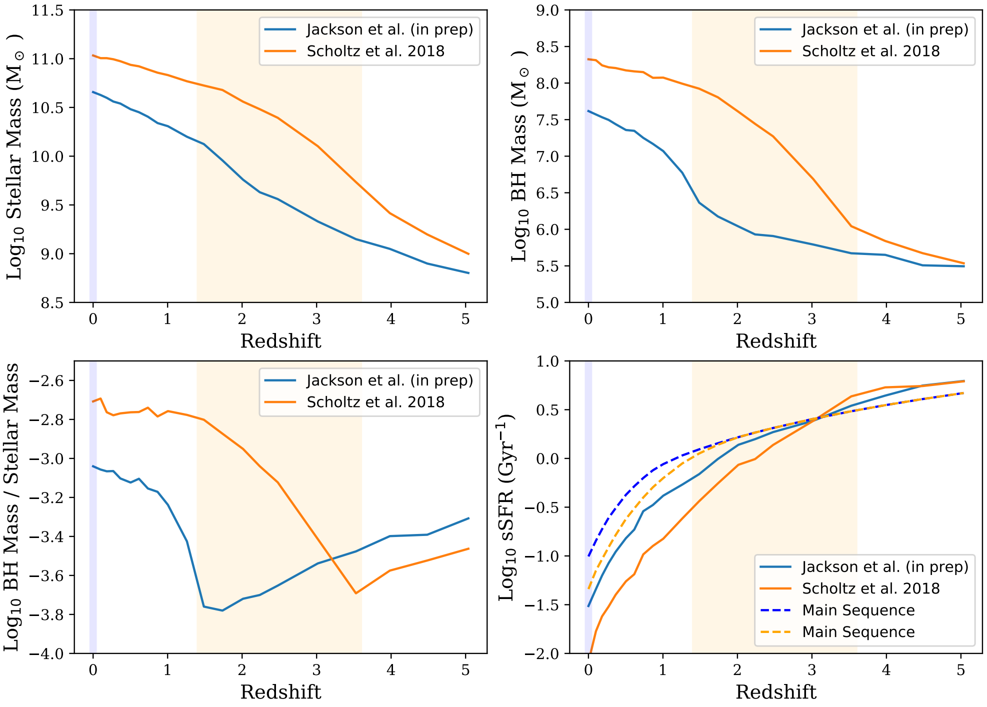

Figure 5.8: The average cosmic evolution from $z = 5$ to $z = 0$ of the Lx AGN sample (blue) and Scholtz AGN sample (orange). The upper left panel shows the median stellar masses, the upper right panel shows the median black hole masses, the bottom left panel median black hole mass over stellar mass and the bottom right panel the median sSFRs and their respective main sequences. The shaded areas show the selection epoch for their respective sample.

for the phase of greatest black hole growth. The bottom right panel confirms that significant differences in the AGN sSFRs and their respective sSFR main sequences occur earlier in the Scholtz AGN. This is a case of downsizing, whereby more massive objects go through physical processes on average earlier. We also see that the phase of most rapid black hole growth occurs at approximately the point at which the SFR drops at it's most rapid rate compared to the main sequence. This indicates that when the black hole is at its most active phase, the feedback energy it is injecting into the surrounding medium is likely to be quenching the SFR.

5.6 Quasar-like episodes in EAGLE

In the previous section, we saw from Figure 5.7 that the median AGN host galaxy SFR follows approximately the star forming main sequence before dropping below the main sequence and remaining there. The most likely cause of the quenching of star formation is AGN feedback. EAGLE delivers AGN feedback thermally, quenching star formation. How the quenching of star formation occurs however, whether immediate or delayed is also important. This could either reveal information which may help with future observational studies or reveal the limitations of the EAGLE simulations. In order to explore the effect of AGN feedback on host galaxy star formation during high level accretion events ($L_{BOL} > 10^{45}$ erg s^{-1}) we used the high time resolution snipshots as described in Section 4.4. The results from the stacking process of the timelines employed to reveal the average BHAR and sSFR behaviour is shown in the left hand panels of Figure 5.9.

We see in the top right panel that the median $\log_{10}$ BHAR before the quasar-like episode is $\simeq 10^{-3}$ $M_{\odot}$ yr^{-1} ($L_{BOL} \simeq 10^{43}$ erg s^{-1}) and that the 14^{th} and 86^{th} percentiles range approximately 2 orders of magnitude. The BHAR then jumps to its maximum of 10^{-1} $M_{\odot}$ yr^{-1} ($L_{BOL} > 10^{45}$ erg s^{-1}) at $t = 0$. After this peak accretion event, the median $\log_{10}$ BHAR then drops 6 orders of magnitude to $\simeq 10^{-5}$ $M_{\odot}$ yr^{-1} ($L_{BOL} \simeq 10^{41}$ erg s^{-1}) and the range of 14^{th} and 86^{th} percentiles is broadened, spanning 6 orders of magnitude. The median BHAR then gradually recovers in the 300 Myrs after to the pre-peak accretion levels and the 14^{th} and 86^{th} percentile range gradually narrows.

The median $\log_{10}$ sSFR (seen as the solid blue line in the bottom right panel) has a fairly constant value of $\simeq -1.5$ before the peak accretion event. This drops an order of magnitude to $\simeq -2.5$ directly after the quasar-like episode. Due to the stochastic nature of star formation in EAGLE, this median value drops intermittently to $-\infty$ after the peak accretion event, indicating over half of our galaxies have no active star formation (SFR $= 0$ $M_{\odot}$ Myr^{-1}) at all at any one timestep. The 86^{th} percentile of the sSFR also drops like the median, however this is a much smaller difference of 0.2 dex, indicating that the behaviour of the sample is not entirely uniform.

To indicate the level of active star formation we plot the fraction of galaxies that form stars at any one time step (bottom right panel). This shows that before the quasar-like event approximately 80% of galaxies formed stars at any one time step. This value drops to approximately 50% immediately after the Quasar-like event. This behaviour indicates a reduction in the amount of galaxies forming stars at any one time may be the main driver of the drop in sSFR.

To check if this is true we plot the top right panel of Figure 5.9. The blue line is the mean SFR per time step for the whole galaxy population, whereas the red line is the mean SFR

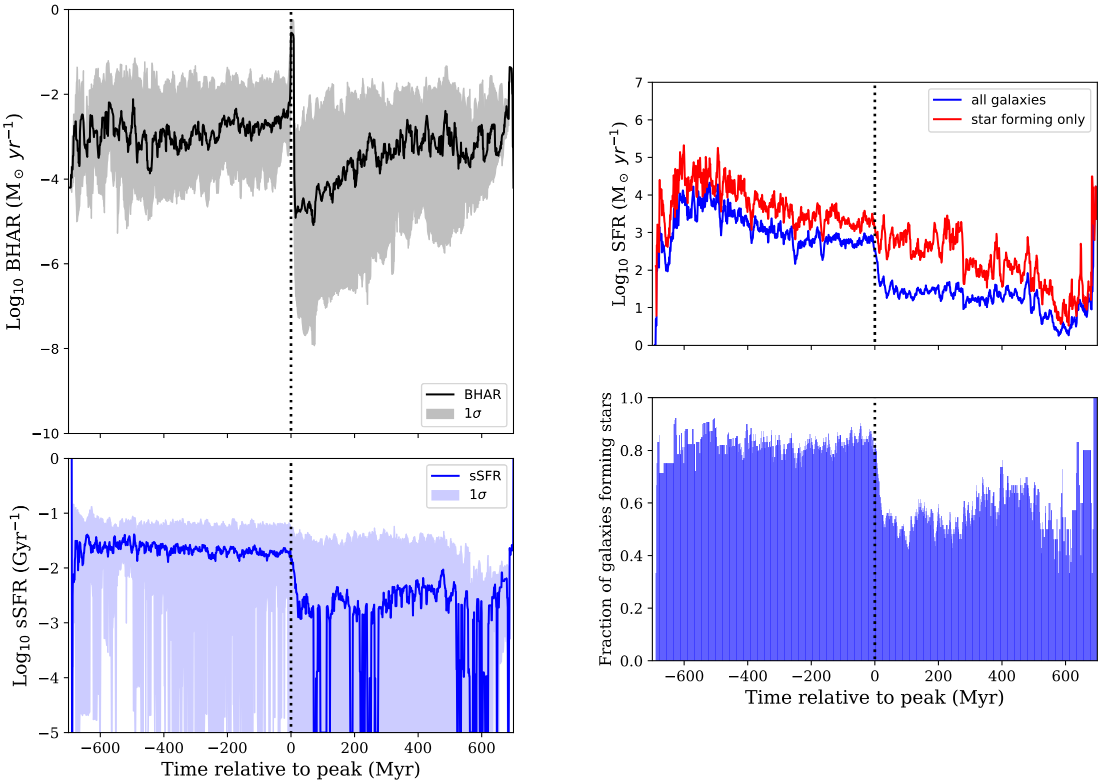

Figure 5.9: The left panels show the median (solid line) and 14th and 86th percentiles (shaded regions) of the BHAR (top) and sSFR (bottom) for every galaxy in EAGLE that underwent a quasar-like ($L_{BOL} > 10^{45}$ erg s^{-1}) phase in the last 700 Myr. The top right panel shows the mean SFR at each individual time step when accounting for the whole population (blue) and only those galaxies which form stars during that time step (red). The bottom right panel shows the fraction of the 89 galaxies which form stars at each individual time step. The black dotted line indicates the peak accretion event at $t = 0$. We see that, on average, at the time of the peak BHAR ($t = 0$), the energy injected thermally by the accretion event has a major and immediate impact on the host galaxy star formation, causing the average sSFR to drop an order of magnitude.

of the subset of galaxies which have any star formation (i.e SFR > 0 M$_\odot$ yr^{-1}) per time step. The blue line shows a major drop in the mean star formation rate at the time of the quasar episode, indicating this is the main driver of the quenching of star formation. The red line, however, indicates that the amount of stars formed in any one episode (i.e per star forming galaxy per time step) gradually decreases from 4.5 M$_\odot$ yr^{-1} to 1.5 M$_\odot$ yr^{-1} over the course of the timelines. So although the quasar episode is the main driver of the quenching of star formation in AGN host galaxies within EAGLE, there is also an additional quenching component over time. Further research of the limitations of these models is beyond the scope of this project and will require further investigation.

Chapter 6

Discussion

In this project, we have taken a sample of hard X-ray selected AGN from the Swift-BAT 58 month catalogue and using multiwavelength photometry, employed SED fitting to find their star forming properties. We then compared these properties to a volume and flux matched sample of AGN from the EAGLE hydrodynamical simulations. We also compared two samples of AGN selected at different epochs in EAGLE, tracking the evolution of various host galaxy properties, and used high time resolution data from EAGLE to explore the mechanisms which quench star formation.

We have seen that the level of agreement between the SFR distributions of our BAT AGN and EAGLE AGN is high, both from the middle of the simulation box and in the MC style methods. The sSFR distributions are not well reproduced, however have similar shapes and both lie below the sSFR main sequence. These points will be discussed initially. We also found from the use of merger trees in EAGLE that AGN selected via similar criteria however at different epochs can display similar behaviour but show different host galaxy properties. This will be discussed next. We have also seen that Quasar-like episodes are a key driver of the quenching of star formation within EAGLE. This is the final point of this discussion.

6.1 Comparison of BAT and EAGLE AGN host galaxy properties

As stated in Section 5.2, we find good agreement between the SFR distributions of our volume and flux matched BAT AGN and EAGLE AGN comparison samples. The statistic recovered from an A-D test gives an probability of 20%. Although not a perfect match, this level of agreement between the SFR distributions suggests a strong likelihood that the two SFR distributions are drawn from the same parent sample, i.e they are likely to be the same. The conclusion drawn from this is reinforced by our MC style methods, which were carried out to verify that an arbitrary point of observation in the simulation box is not biased. The distribution of p-values recovered had a median 45% agreement. This level of agreement helps justify our conclusion that EAGLE reproduces the observed SFR distribution of local AGN, regardless of the point of observation in the simulation box.

A comparison of the BAT AGN and EAGLE AGN X-ray luminosity distributions shows that EAGLE does not appear to reproduce as higher luminosities as observed, although the range of X-ray luminosities is exactly the same for both samples. Indeed when an A-D test is run on the BAT AGN and EAGLE AGN $L_{14-195keV}$ distributions we find a 1.8% chance that the two are drawn from the same parent sample. We postulate, however, that this discrepancy may be due to the short timescales of which AGN activity varies. This can be seen from the high time resolution snipshots in EAGLE, which show the dramatic variation in the BHAR (many orders of magnitude) over short time scales. By considering these snipshots, we find 89 objects which undergo at least one quasar like phase ($L_{BOL} > 10^{45}$ erg s^{-1}) in the last 700 Myr. This indicates that EAGLE can replicate the luminosities of our observational sample and that it is likely that the short timescales of AGN variability that is responsible for the lack of matching in these two AGN X-ray luminosity distributions. This may also depend on the assumptions we made earlier such as the value of the radiative efficiency, ϵ. If we were to take a higher value (i.e 15% or 20%) then we would expect the X-ray luminosities to be much higher. With our flux matching we would expect many more X-ray sources, which may be unlikely. This would however, be likely to introduce greater numbers of less massive sources, which may have higher sSFRs. This would then have to be reconciled with the compton thick sources (below).

The sSFR distributions are less well produced. This appears to be due to EAGLE, on average, overpredicting the stellar masses of AGN host galaxies. The exact reason for this is unknown, however will be investigated in future work. The median of the sSFR distribution from the BAT AGN appears to lie below the sSFR main sequence and above the average galaxy population in EAGLE, in good agreement with Scholtz et al. (2018). One assumption made here is that an offset of 0.2 dex in the SFRs needs to be applied to all the EAGLE galaxies, as seen by Furlong et al. (2015). This shows that there is already limitations in EAGLEs reproduction of SFRs, which could be further explored and provide the explanation for the differences seen.

One point to consider is that although Swift-BAT does detect many heavily obscured AGN, some compton thick sources may be missed. This explantion could account for some of the disparities in the different amounts of BAT and EAGLE AGN. Ricci et al. (2015) find that compton thick AGN may account for $\approx 46\%$ of AGN in the X-ray luminosity range Log_{10} $\mathrm{L}_{14-195keV} = 40 - 43.7$ and $\approx 39\%$ for Log_{10} $\mathrm{L}_{14-195keV} = 43.7 - 46$. When taking into account the statistic for the lower luminosity range, which better fits our sample, we find the expected AGN count in the BAT AGN sample is 133, almost exactly the same as our EAGLE AGN sample. Heavy obscuration preferentially removes lower luminosity objects, which may account for some of the differences in the X-ray luminosity distributions. This should not effect the SFR distributions, however the sSFR distributions may be higher in compton thick sources due to their on average higher sSFRs driven by their gas rich nature. The full effects of including compton thick sources in our comparison however is beyond the scope of this thesis.

6.2 How the host galaxies of AGN selected at different epochs differ

From our use of the merger trees for two differently selected AGN samples ($\mathrm{L}_{14-195keV} > 10^{42}$ erg s^{-1} at $z = 0$ compared to Scholtz et al. (2018) where $\mathrm{L}_x > 10^{43}$ erg s^{-1} at $1.4 < z < 3.6$), we see how the selection criteria can affect the host galaxy evolution. The results are shown in Figure 5.7 and Figure 5.8.

Downsizing, whereby less massive objects undergo physical processes later in the history of the universe, is clearly displayed in the SFRs in Figure 5.7. The AGN sample selected via luminosity cut (Section 4.3) from this work (which have smaller stellar masses across all ages) on average leave the main sequence in star formation later than the Scholtz AGN. Downsizing is also displayed in the bottom panels of Figure 5.8 where the black hole mass to stellar mass ratio experiences its greatest growth and the sSFR deviates significantly from the main sequence later in the sample from this work in comparison to the Scholtz AGN.

By comparing Figure 5.7 and Figure 5.8 we see that the star formation starts deviating from the main sequence for both our AGN sample and the Scholtz AGN when the stellar masses reach a critical point of $\mathrm{M}_* \approx 10^{10}$ $\mathrm{M}_\odot$. McAlpine et al. (2017) explain that this is due the host galaxy having attained enough mass that stellar and supernovae feedback can no longer keep ejecting gas from the galaxy and gas starts flowing into the centre of the galaxy, accreting around the black hole.

We also find some overlap in our objects with those of Scholtz et al. (2018). This indicates that a galaxy in EAGLE that underwent a significant AGN episode at earlier redshifts ($z > 1.5$) still has the potential to undergo a separate, unrelated AGN episode at $z = 0$. This could be related to environment where mergers may trigger a secondary episode of AGN activity, although more work would need to be carried out to investigate this.

Finally we find that although the median SFR of the EAGLE AGN sample selected by a luminosity cut and the Scholtz EAGLE AGN sample are similar and the selections are fairly similar, the average present day ($z = 0$) host galaxy properties display differences. Our AGN sample has an average $\log_{10}$ sSFR 0.5 dex higher, an average stellar mass 0.4 dex smaller, an average black hole mass 0.8 dex smaller and 0.3 dex black hole mass to stellar mass ratio smaller than the average galaxy from the Scholtz AGN sample. This shows that although AGN can be selected using similar criteria and can display very similar behaviour, they can have different present day host galaxy properties.

6.3 How quasar-like episodes affect Star Formation in EAGLE

Figure 5.9 shows that quasar-like events ($L_{BOL} > 10^{45}$ erg s^{-1}) in EAGLE can have a significant effect on the host galaxy, disrupting both the black hole accretion and the star formation immediately afterwards. This suggests a scenario in EAGLE whereby, on average, the BHAR in an object peaks and temporarily injects enough energy into the surrounding material within the galaxy to warm the gas to a high enough temperature that black hole accretion and star formation are supressed. The BHAR recovers after a period of approximately $\approx$ 300 Myr, however the sSFR does not. The black hole then accretes at the same rate as before the quasar episode after this period of suppression, indicating that the average AGN galaxy may have the potential to undergo multiple quasar-like episodes in its lifetime. This is to be expected from the model applied to EAGLE, however we also find that although the main driver of star formation quenching arises from these quasar-like events, there is also another component, whereby the star formation quenches over time. The exact source of this quenching is undoubtely other accretion events, however the minimum amount of energy needed to quench star formation and other conditions which are needed to quench star formation will need to be investigated in further research.

Chapter 7

Conclusion

This project has compared the star forming properties of a sample of low redshift, hard X-ray selected AGN from the Swift-BAT all-sky survey. We compared the SFR distribution, sSFR distribution and position on the sSFR main sequence of this observational sample to a volume matched, flux matched sample of AGN from the EAGLE hydrodynamical suite of simulations.

We find a good level of agreement in the SFR distributions, with an Anderson-Darling test recovering a 20% agreement between the observational and simulated AGN samples as observed from the centre of the simulation box. To verify that an arbitrary point in the simulation box is not biased we ran some MC style methods, randomising the redshifts of galaxies within EAGLE. The distribution in the values of the levels of agreement yielded a median value of 45 ± 15%.

The sSFR distributions are not in agreement, as EAGLE appears to underpredict the sSFRs of the AGN comparison sample. This is due to an overprediction of the AGN host galaxy stellar masses. The observed BAT AGN appear to lie below the sSFR main sequence, however above the average EAGLE galaxy population, in good agreement with the results found from Scholtz et al. (2018). The X-ray luminosity distributions are also less well reproduced. This, however, may be due to the short variability timescales of AGN activity. The amount of compton thick AGN may also provide an explantion in the some of the differences seen, however this is beyond the scope of this current work.

We compared the cosmic evolution of the host galaxy properties of a sample of AGN from EAGLE selected at $z = 0$ with $L_{14-195keV} > 10^{42}$ erg s^{-1} with the EAGLE AGN sample from Scholtz et al. (2018). We find that a surprisingly significant number of AGN (50/290) observed at earlier redshifts from Scholtz et al. (2018) may still undergo a significant accretion event in the present day. We find that within EAGLE, star formation is indeed quenched over time, with this mechanism starting at a critical host galaxy stellar mass of $\simeq 10^{10}$ $M_{\odot}$. We also find that AGN selected on similar properties but at different epochs display similar evolutionary behaviours, however, have different present day host galaxy properties. Finally by using high resolution snapshots in EAGLE, we find that Quasar-like events can significantly supress star formation within their host galaxies.

Acknowledgements

I, Thomas M. Jackson would like to thank the following people:

Firstly my two supervisors Prof. David Alexander and Dr. David Rosario for providing me with direction throughout this project, helping me when I needed it and channeling my energy. Secondly my research group for always being there with helpful advice, especially around lunch. Thirdly Mr Stuart McAlpine and Prof Richard Bower for their invaluable help and extensive knowledge of the EAGLE simulations. Finally my girlfriend Paulina, for putting up with me and my work throughout this year.

I would also like to acknowledge the Pemberton Fund from the Durham Castle Society and the Leather Sellers guild for their generosity in granting me bursaries which helped me finance my Masters by Research. Without this financial aid, I would not have been able to undertake a masters degree.

This project used data from the Sloan Digital Sky survey, funded by the Alfred P. Sloan Foundation, the U.S. Department of Energy Office of Science, and the Participating Institutions.

This project used data from 2MASS survey, a collaboration between The University of Massachusetts and the Infrared Processing and Analysis Center (JPL/ Caltech). Funding is provided primarily by NASA and the NSF.

This publication makes use of data products from the Wide-field Infrared Survey Explorer, which is a joint project of the University of California, Los Angeles, and the Jet Propulsion Laboratory/California Institute of Technology, funded by the National Aeronautics and Space Administration.

This project used data from the HyperLeda database (http://leda.univ-lyon1.fr).

This project used data from the NASA Sloan Atlas database. Funding for the NASA-Sloan Atlas has been provided by the NASA Astrophysics Data Analysis Program (08-ADP08-0072) and the NSF (AST-1211644).

This project used data from Pan-STARRs. The Pan-STARRS1 Surveys (PS1) and the PS1 public science archive have been made possible through contributions by the Institute for Astronomy, the University of Hawaii, the Pan-STARRS Project Office, the Max-Planck Society and all other associated institutions found on the database website.

This project used data from the NASA Extragalactic database. Funded by NASA and other associated institutes.

This work used the DiRAC Data Centric system at Durham University, operated by the Institute for Computational Cosmology on behalf of the STFC DiRAC HPC Facility. This equipment was funded by BIS National E-infrastructure capital grant ST/K00042X/1, STFC capital grant ST/H008519/1, and STFC DiRAC Operations grant ST/K003267/1 and Durham University. DiRAC is part of the National E-Infrastructure.

Appendix A

SED fits

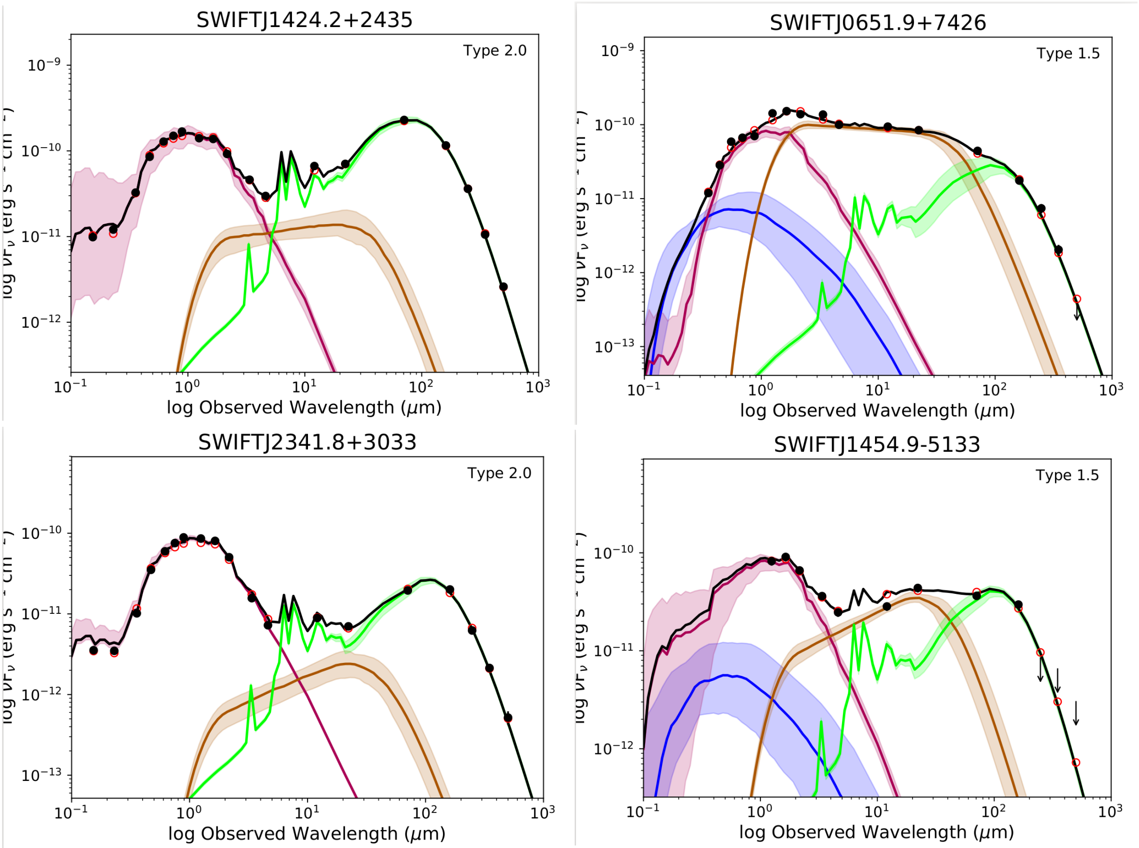

Figure A.1: A sub sample of the SED fits. The black points are the photometric points collected, with upper limits represented by arrows. The black line represents the fully fitted SED, green represents the emission component produced by from dust in the galaxy, red emission from stars, orange emission from the AGN torus and blue UV emission from the accretion disk. At the top is the Swift-BAT ID of the respective galaxy and the pre-determined type of each AGN from the BASS database can be found in the top corner.

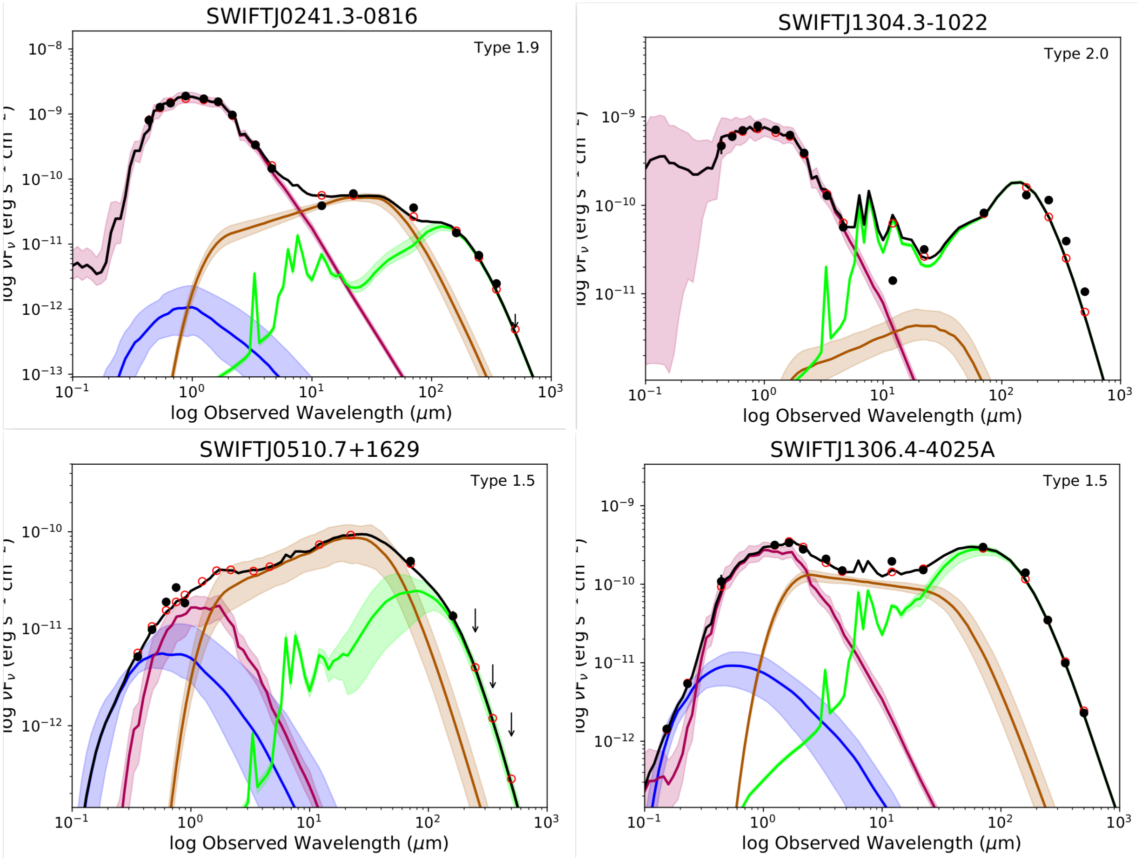

Figure A.2: Continuation of Figure A.1.

Appendix B

Initial Comparison Graphs

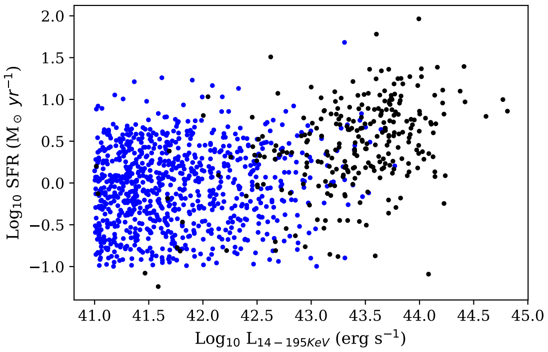

Figure B.1: SFR versus X-ray luminosity for the full BAT AGN sample (black) and a luminosity cut ($L_{14-195KeV} > 10^{41}$ erg s^{-1}) in EAGLE (blue). As can be seen, there is relatively little overlap between the two samples.

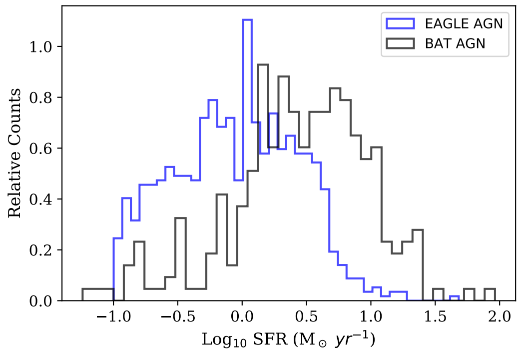

Figure B.2: An initial comparison of the SFR distributions of the unmatched full BAT AGN sample and EAGLE (taken from a luminosity cut of ($L_{14-195KeV} > 10^{41}$ erg s^{-1})).

Appendix C

Colour-Magnitude diagram

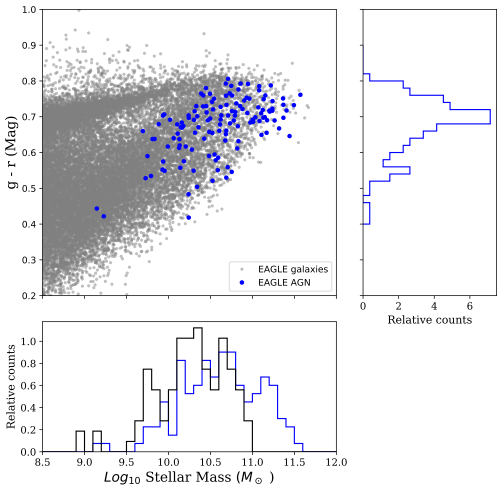

Figure C.1: A colour magnitude diagram for all EAGLE galaxies (grey) and the EAGLE AGN sample (blue). The stellar mass distributions of the EAGLE AGN (blue) and BAT AGN (black) are found in the bottom panel.

Bibliography

Aird, J., A. L. Coil, A. Georgakakis, K. Nandra, G. Barro, and P. G. Pérez-González
2015. The evolution of the X-ray luminosity functions of unabsorbed and absorbed AGNs out to z = 5. MNRAS, 451:1892–1927.

Alexander, D. M., W. N. Brandt, A. E. Hornschemeier, G. P. Garmire, D. P. Schneider, F. E. Bauer, and R. E. Griffiths
2001. The Chandra Deep Field North Survey. VI. The Nature of the Optically Faint X-Ray Source Population. AJ, 122:2156–2176.

Alexander, D. M. and R. C. Hickox
2012. What drives the growth of black holes? New A Rev., 56:93–121.

Bower, R. G., A. J. Benson, R. Malbon, J. C. Helly, C. S. Frenk, C. M. Baugh, S. Cole, and C. G. Lacey
2006. Breaking the hierarchy of galaxy formation. MNRAS, 370:645–655.

Bower, R. G., J. Schaye, C. S. Frenk, T. Theuns, M. Schaller, R. A. Crain, and S. McAlpine
2017. The dark nemesis of galaxy formation: why hot haloes trigger black hole growth and bring star formation to an end. MNRAS, 465:32–44.

Chabrier, G.
2003. Galactic Stellar and Substellar Initial Mass Function. PASP, 115:763–795.

Corwin, Jr., H. G., R. J. Buta, and G. de Vaucouleurs
1994. Corrections and additions to the third reference catalogue of bright galaxies. AJ, 108:2128–2144.

Courteau, S., M. Cappellari, R. S. de Jong, A. A. Dutton, E. Emsellem, H. Hoekstra, L. V. E. Koopmans, G. A. Mamon, C. Maraston, T. Treu, and L. M. Widrow
2014. Galaxy masses. *Reviews of Modern Physics*, 86:47–119.

Crain, R. A., J. Schaye, R. G. Bower, M. Furlong, M. Schaller, T. Theuns, C. Dalla Vecchia, C. S. Frenk, I. G. McCarthy, J. C. Helly, A. Jenkins, Y. M. Rosas-Guevara, S. D. M. White, and J. W. Trayford
2015. The EAGLE simulations of galaxy formation: calibration of subgrid physics and model variations. MNRAS, 450:1937–1961.

Croton, D. J., V. Springel, S. D. M. White, G. De Lucia, C. S. Frenk, L. Gao, A. Jenkins, G. Kauffmann, J. F. Navarro, and N. Yoshida
2006. Erratum: The many lives of active galactic nuclei: cooling flows, black holes and the luminosities and colours of galaxies. MNRAS, 367:864–864.

de Vaucouleurs, G.
1991. On the distribution of radio sources in rich galaxy clusters. MNRAS, 249:28P–30P.

Dubois, Y., S. Peirani, C. Pichon, J. Devriendt, R. Gavazzi, C. Welker, and M. Volonteri
2016. The HORIZON-AGN simulation: morphological diversity of galaxies promoted by AGN feedback. MNRAS, 463:3948–3964.

Fabian, A. C.
2012. Observational Evidence of Active Galactic Nuclei Feedback. ARA&A, 50:455–489.

Furlong, M., R. G. Bower, T. Theuns, J. Schaye, R. A. Crain, M. Schaller, C. Dalla Vecchia, C. S. Frenk, I. G. McCarthy, J. Helly, A. Jenkins, and Y. M. Rosas-Guevara
2015. Evolution of galaxy stellar masses and star formation rates in the EAGLE simulations. MNRAS, 450:4486–4504.

Hardcastle, M. J.
2018. A simulation-based analytic model of radio galaxies. MNRAS, 475:2768–2786.

Häring, N. and H.-W. Rix
2004. On the Black Hole Mass-Bulge Mass Relation. ApJ, 604:L89–L92.

Harrison, C. M.
2017. Impact of supermassive black hole growth on star formation. *Nature Astronomy*, 1:0165.

Harrison, C. M., D. M. Alexander, J. R. Mullaney, B. Altieri, D. Coia, V. Charmandaris, E. Daddi, H. Dannerbauer, K. Dasyra, A. Del Moro, M. Dickinson, R. C. Hickox, R. J. Ivison, J. Kartaltepe, E. Le Floc'h, R. Leiton, B. Magnelli, P. Popesso, E. Rovilos, D. Rosario,

and A. M. Swinbank
2012. No Clear Submillimeter Signature of Suppressed Star Formation among X-Ray Luminous Active Galactic Nuclei. ApJ, 760:L15.

Hickox, R. C., J. R. Mullaney, D. M. Alexander, C.-T. J. Chen, F. M. Civano, A. D. Goulding, and K. N. Hainline
2014. Black Hole Variability and the Star Formation-Active Galactic Nucleus Connection: Do All Star-forming Galaxies Host an Active Galactic Nucleus? ApJ, 782:9.

Ho, L. C., Z.-Y. Li, A. J. Barth, M. S. Seigar, and C. Y. Peng
2011. The Carnegie-Irvine Galaxy Survey. I. Overview and Atlas of Optical Images. ApJS, 197:21.

Kelly, B. C.
2007. Some Aspects of Measurement Error in Linear Regression of Astronomical Data. ApJ, 665:1489–1506.

Kennicutt, R. C. and N. J. Evans
2012. Star Formation in the Milky Way and Nearby Galaxies. ARA&A, 50:531–608.

Kormendy, J. and L. C. Ho
2013. Coevolution (Or Not) of Supermassive Black Holes and Host Galaxies. ARA&A, 51:511–653.

Koss, M., R. Mushotzky, S. Veilleux, and L. Winter
2010. Merging and Clustering of the Swift BAT AGN Sample. ApJ, 716:L125–L130.

Lacey, C. G., C. M. Baugh, C. S. Frenk, A. J. Benson, R. G. Bower, S. Cole, V. Gonzalez-Perez, J. C. Helly, C. D. P. Lagos, and P. D. Mitchell
2016. A unified multiwavelength model of galaxy formation. MNRAS, 462:3854–3911.

Lagos, C. d. P., R. A. Crain, J. Schaye, M. Furlong, C. S. Frenk, R. G. Bower, M. Schaller, T. Theuns, J. W. Trayford, Y. M. Bahé, and C. Dalla Vecchia
2015. Molecular hydrogen abundances of galaxies in the EAGLE simulations. MNRAS, 452:3815–3837.

McAlpine, S., R. G. Bower, C. M. Harrison, R. A. Crain, M. Schaller, J. Schaye, and T. Theuns
2017. The link between galaxy and black hole growth in the eagle simulation. MNRAS, 468:3395–3407.

McAlpine, S., J. C. Helly, M. Schaller, J. W. Trayford, Y. Qu, M. Furlong, R. G. Bower, R. A. Crain, J. Schaye, T. Theuns, C. Dalla Vecchia, C. S. Frenk, I. G. McCarthy, A. Jenkins, Y. Rosas-Guevara, S. D. M. White, M. Baes, P. Camps, and G. Lemson
2016. The EAGLE simulations of galaxy formation: Public release of halo and galaxy catalogues. *Astronomy and Computing*, 15:72–89.

Meléndez, M., R. F. Mushotzky, T. T. Shimizu, A. J. Barger, and L. L. Cowie
2014. Herschel Far-infrared Photometry of the Swift Burst Alert Telescope Active Galactic Nuclei Sample of the Local Universe. I. PACS Observations. ApJ, 794:152.

Netzer, H.
2009. Accretion and star formation rates in low-redshift type II active galactic nuclei. MNRAS, 399:1907–1920.

Netzer, H., D. Lutz, M. Schweitzer, A. Contursi, E. Sturm, L. J. Tacconi, S. Veilleux, D.-C. Kim, D. Rupke, A. J. Baker, K. Dasyra, J. Mazzarella, and S. Lord
2007. Spitzer Quasar and ULIRG Evolution Study (QUEST). II. The Spectral Energy Distributions of Palomar-Green Quasars. ApJ, 666:806–816.

Page, M. J., M. Symeonidis, J. D. Vieira, B. Altieri, A. Amblard, V. Arumugam, H. Aussel, T. Babbedge, A. Blain, J. Bock, A. Boselli, V. Buat, N. Castro-Rodríguez, A. Cava, P. Chanial, D. L. Clements, A. Conley, L. Conversi, A. Cooray, C. D. Dowell, E. N. Dubois, J. S. Dunlop, E. Dwek, S. Dye, S. Eales, D. Elbaz, D. Farrah, M. Fox, A. Franceschini, W. Gear, J. Glenn, M. Griffin, M. Halpern, E. Hatziminaoglou, E. Ibar, K. Isaak, R. J. Ivison, G. Lagache, L. Levenson, N. Lu, S. Madden, B. Maffei, G. Mainetti, L. Marchetti, H. T. Nguyen, B. O'Halloran, S. J. Oliver, A. Omont, P. Panuzzo, A. Papageorgiou, C. P. Pearson, I. Pérez-Fournon, M. Pohlen, J. I. Rawlings, D. Rigopoulou, L. Riguccini, D. Rizzo, G. Rodighiero, I. G. Roseboom, M. Rowan-Robinson, M. S. Portal, B. Schulz, D. Scott, N. Seymour, D. L. Shupe, A. J. Smith, J. A. Stevens, M. Trichas, K. E. Tugwell, M. Vaccari, I. Valtchanov, M. Viero, L. Vigroux, L. Wang, R. Ward, G. Wright, C. K. Xu, and M. Zemcov
2012. The suppression of star formation by powerful active galactic nuclei. Nature, 485:213–216.

Planck Collaboration, Fermi Collaboration, P. A. R. Ade, N. Aghanim, G. Aniano, M. Arnaud, M. Ashdown, J. Aumont, C. Baccigalupi, A. J. Banday, R. B. Barreiro, N. Bartolo, E. Battaner, K. Benabed, A. Benoit-Lévy, J.-P. Bernard, M. Bersanelli, P. Bielewicz,

A. Bonaldi, L. Bonavera, J. R. Bond, J. Borrill, F. R. Bouchet, F. Boulanger, C. Burigana, R. C. Butler, E. Calabrese, J.-F. Cardoso, J. M. Casandjian, A. Catalano, A. Chamballu, H. C. Chiang, P. R. Christensen, L. P. L. Colombo, C. Combet, F. Couchot, B. P. Crill, A. Curto, F. Cuttaia, L. Danese, R. D. Davies, R. J. Davis, P. de Bernardis, A. de Rosa, G. de Zotti, J. Delabrouille, F.-X. Désert, C. Dickinson, J. M. Diego, S. W. Digel, H. Dole, S. Donzelli, O. Doré, M. Douspis, A. Ducout, X. Dupac, G. Efstathiou, F. Elsner, T. A. Enßlin, H. K. Eriksen, E. Falgarone, F. Finelli, O. Forni, M. Frailis, A. A. Fraisse, E. Franceschi, A. Frejsel, Y. Fukui, S. Galeotta, S. Galli, K. Ganga, T. Ghosh, M. Giard, E. Gjerløw, J. González-Nuevo, K. M. Górski, A. Gregorio, I. A. Grenier, A. Gruppuso, F. K. Hansen, D. Hanson, D. L. Harrison, S. Henrot-Versillé, C. Hernández-Monteagudo, D. Herranz, S. R. Hildebrandt, E. Hivon, M. Hobson, W. A. Holmes, W. Hovest, K. M. Huffenberger, G. Hurier, A. H. Jaffe, T. R. Jaffe, W. C. Jones, M. Juvela, E. Keihänen, R. Keskitalo, T. S. Kisner, R. Kneissl, J. Knoche, M. Kunz, H. Kurki-Suonio, G. Lagache, J.-M. Lamarre, A. Lasenby, M. Lattanzi, C. R. Lawrence, R. Leonardi, F. Levrier, M. Liguori, P. B. Lilje, M. Linden-Vørnle, M. López-Caniego, P. M. Lubin, J. F. Macías-Pérez, B. Maffei, D. Maino, N. Mandolesi, M. Maris, D. J. Marshall, P. G. Martin, E. Martínez-González, S. Masi, S. Matarrese, P. Mazzotta, A. Melchiorri, L. Mendes, A. Mennella, M. Migliaccio, M.-A. Miville-Deschênes, A. Moneti, L. Montier, G. Morgante, D. Mortlock, D. Munshi, J. A. Murphy, P. Naselsky, P. Natoli, H. U. Nørgaard-Nielsen, D. Novikov, I. Novikov, C. A. Oxborrow, L. Pagano, F. Pajot, R. Paladini, D. Paoletti, F. Pasian, O. Perdereau, L. Perotto, F. Perrotta, V. Pettorino, F. Piacentini, M. Piat, S. Plaszczynski, E. Pointecouteau, G. Polenta, L. Popa, G. W. Pratt, S. Prunet, J.-L. Puget, J. P. Rachen, W. T. Reach, R. Rebolo, M. Reinecke, M. Remazeilles, C. Renault, I. Ristorcelli, G. Rocha, G. Roudier, B. Rusholme, M. Sandri, D. Santos, D. Scott, L. D. Spencer, V. Stolyarov, A. W. Strong, R. Sudiwala, R. Sunyaev, D. Sutton, A.-S. Suur-Uski, J.-F. Sygnet, J. A. Tauber, L. Terenzi, L. Tibaldo, L. Toffolatti, M. Tomasi, M. Tristram, M. Tucci, G. Umana, L. Valenziano, J. Valiviita, B. Van Tent, P. Vielva, F. Villa, L. A. Wade, B. D. Wandelt, I. K. Wehus, D. Yvon, A. Zacchei, and A. Zonca
2015. Planck intermediate results. XXVIII. Interstellar gas and dust in the Chamaeleon clouds as seen by Fermi LAT and Planck. A&A, 582:A31.

Prugniel, P. and P. Heraudeau
1998. Total magnitude, radius, colour indices, colour gradients and photometric type of galaxies. A&AS, 128:299–308.

Ricci, C., Y. Ueda, M. J. Koss, B. Trakhtenbrot, F. E. Bauer, and P. Gandhi
2015. Compton-thick Accretion in the Local Universe. ApJ, 815:L13.

Richstone, D., E. A. Ajhar, R. Bender, G. Bower, A. Dressler, S. M. Faber, A. V. Filippenko, K. Gebhardt, R. Green, L. C. Ho, J. Kormendy, T. R. Lauer, J. Magorrian, and S. Tremaine
1998. Supermassive black holes and the evolution of galaxies. Nature, 395:A14.

Rosario, D. J., P. Santini, D. Lutz, L. Shao, R. Maiolino, D. M. Alexander, B. Altieri, P. Andreani, H. Aussel, F. E. Bauer, S. Berta, A. Bongiovanni, W. N. Brandt, M. Brusa, J. Cepa, A. Cimatti, T. J. Cox, E. Daddi, D. Elbaz, A. Fontana, N. M. Förster Schreiber, R. Genzel, A. Grazian, E. Le Floch, B. Magnelli, V. Mainieri, H. Netzer, R. Nordon, I. Pérez Garcia, A. Poglitsch, P. Popesso, F. Pozzi, L. Riguccini, G. Rodighiero, M. Salvato, M. Sanchez-Portal, E. Sturm, L. J. Tacconi, I. Valtchanov, and S. Wuyts
2012. The mean star formation rate of X-ray selected active galaxies and its evolution from z ˜ 2.5: results from PEP-Herschel. A&A, 545:A45.

Sartori, L. F., K. Schawinski, B. Trakhtenbrot, N. Caplar, E. Treister, M. J. Koss, C. M. Urry, and C. E. Zhang
2018. A model for AGN variability on multiple time-scales. MNRAS, 476:L34–L38.

Schaller, M., C. S. Frenk, R. G. Bower, T. Theuns, A. Jenkins, J. Schaye, R. A. Crain, M. Furlong, C. Dalla Vecchia, and I. G. McCarthy
2015. Baryon effects on the internal structure of ΛCDM haloes in the EAGLE simulations. MNRAS, 451:1247–1267.

Schaye, J., R. A. Crain, R. G. Bower, M. Furlong, M. Schaller, T. Theuns, C. Dalla Vecchia, C. S. Frenk, I. G. McCarthy, J. C. Helly, A. Jenkins, Y. M. Rosas-Guevara, S. D. M. White, M. Baes, C. M. Booth, P. Camps, J. F. Navarro, Y. Qu, A. Rahmati, T. Sawala, P. A. Thomas, and J. Trayford
2015. The EAGLE project: simulating the evolution and assembly of galaxies and their environments. MNRAS, 446:521–554.

Schaye, J. and C. Dalla Vecchia
2008. On the relation between the Schmidt and Kennicutt-Schmidt star formation laws and its implications for numerical simulations. MNRAS, 383:1210–1222.

Scholtz, J., D. M. Alexander, C. M. Harrison, D. J. Rosario, S. McAlpine, J. R. Mullaney, F. Stanley, J. Simpson, T. Theuns, R. G. Bower, R. C. Hickox, P. Santini, and A. M.

Swinbank
2018. Identifying the subtle signatures of feedback from distant AGN using ALMA observations and the EAGLE hydrodynamical simulations. MNRAS, 475:1288–1305.

Schreiber, C., M. Pannella, D. Elbaz, M. Béthermin, H. Inami, M. Dickinson, B. Magnelli, T. Wang, H. Aussel, E. Daddi, S. Juneau, X. Shu, M. T. Sargent, V. Buat, S. M. Faber, H. C. Ferguson, M. Giavalisco, A. M. Koekemoer, G. Magdis, G. E. Morrison, C. Papovich, P. Santini, and D. Scott
2015. The Herschel view of the dominant mode of galaxy growth from z = 4 to the present day. A&A, 575:A74.

Shimizu, T. T., M. Meléndez, R. F. Mushotzky, M. J. Koss, A. J. Barger, and L. L. Cowie
2016. Herschel far-infrared photometry of the Swift Burst Alert Telescope active galactic nuclei sample of the local universe - II. SPIRE observations. MNRAS, 456:3335–3353.

Shimizu, T. T., R. F. Mushotzky, M. Meléndez, M. J. Koss, A. J. Barger, and L. L. Cowie
2017. Herschel far-infrared photometry of the Swift Burst Alert Telescope active galactic nuclei sample of the local universe - III. Global star-forming properties and the lack of a connection to nuclear activity. MNRAS, 466:3161–3183.

Springel, V.
2005. The cosmological simulation code GADGET-2. MNRAS, 364:1105–1134.

Stanley, F., D. M. Alexander, C. M. Harrison, D. J. Rosario, L. Wang, J. A. Aird, N. Bourne, L. Dunne, S. Dye, S. Eales, K. K. Knudsen, M. J. Michałowski, E. Valiante, G. De Zotti, C. Furlanetto, R. Ivison, S. Maddox, and M. W. L. Smith
2017. The mean star formation rates of unobscured QSOs: searching for evidence of suppressed or enhanced star formation. MNRAS, 472:2221–2240.

Stanley, F., C. M. Harrison, D. M. Alexander, A. M. Swinbank, J. A. Aird, A. Del Moro, R. C. Hickox, and J. R. Mullaney
2015. A remarkably flat relationship between the average star formation rate and AGN luminosity for distant X-ray AGN. MNRAS, 453:591–604.

Trayford, J. W., T. Theuns, R. G. Bower, J. Schaye, M. Furlong, M. Schaller, C. S. Frenk, R. A. Crain, C. Dalla Vecchia, and I. G. McCarthy
2015. Colours and luminosities of z = 0.1 galaxies in the EAGLE simulation. MNRAS, 452:2879–2896.

van den Bosch, R. C. E.

2016. Unification of the fundamental plane and Super Massive Black Hole Masses. ApJ, 831:134.